12-2009

Age Effects on Iron-Based Pipes in Water Distribution Systems

Ryan T. Christensen
Utah State University

AGE EFFECTS ON IRON-BASED PIPES IN

WATER DISTRIBUTION SYSTEMS

by

Ryan T. Christensen

A dissertation submitted in partial fulfillment
of the requirements for the degree

of

DOCTOR OF PHILOSOPHY

in

Civil and Environmental Engineering

Approved:

William J. Rahmeyer Major Professor	Steven L. Barfuss Committee Member
Michael C. Johnson Committee Member	Laurie S. McNeill Committee Member
Robert E. Spall Committee Member	Byron R. Burnham Dean of Graduate Studies

UTAH STATE UNIVERSITY
Logan, Utah

2009

ABSTRACT

Age Effects on Iron-Based Pipes

in Distribution Systems

by

Ryan T. Christensen, Doctor of Philosophy

Utah State University, 2009

Major Professor: William J. Rahmeyer
Department: Civil and Environmental Engineering

Pipes in water distribution systems may change as they age. The accumulation of corrosion byproducts and suspended particles on the inside wall of aged pipes can increase pipe roughness and reduce pipe diameter. To quantify the hydraulic effects of irregular accumulation on the pipe walls, eleven aged pipes ranging in diameter from 0.020-m (0.75-in) to 0.100-m (4-in) and with varying degrees of turberculation were located and subjected to laboratory testing. The laboratory test results were used to determine a relationship between pipe diameter reduction and Hazen-Williams C. This relationship, combined with a manipulation of the Hazen-Williams equation, provided a simple and direct method for correcting the diameters of aged pipes in distribution models. Using EPANET 2, the importance of correcting pipe diameters when modeling water distribution systems containing aged pipes was investigated. Correcting the pipe

diameters in the sample network reduced the modeled water age by up to 10% and changed the pattern of fluctuating water age that occurred as waters with different sources moved through the pipe network.

In addition, two of the aforementioned aged pipes with diameters of 0.025-m (1-in) and 0.050-m (2-in) were modeled using Reynolds-Averaged Navier-Stokes (RANS) turbulence modeling. Flow was computed at Reynolds numbers ranging from 6700 to 31,000 using three turbulence models including a 4-equation $v^2 - f$ model, and 2-equation realizable $k - \varepsilon$ and $k - \omega$ models. In comparing the RANS results to the laboratory testing, the $v^2 - f$ model was found to be most accurate, producing Darcy-Weisbach friction factors from 5% higher to 15% lower than laboratory-obtained values. The capability of RANS modeling to provide a detailed characterization of the flow in aged pipes was demonstrated.

Large eddy simulation (LES) was also performed on a single 0.050-m (2-in) pipe at a Reynolds number of 6800. The Darcy-Weisbach friction factor calculated using LES was 20% less than obtained from experimental tests. Roughness elements smaller than the grid scale and deficiencies in the subgrid-scale model at modeling the complex three-dimensional flow structures due to the irregular pipe boundary were identified as likely sources of error. Even so, the utility of LES for describing complex flows was established.

(108 pages)

ACKNOWLEDGMENTS

First, I would like to thank Steve Barfuss, who has acted as my research mentor and directed my dissertation study. Without his support and tireless work on my behalf, this project would have never been possible. Bob Spall also deserves special credit as he has been my CFD mentor and primary reviewer for the sections of this work devoted to CFD. Bill Rahmeyer, Mike Johnson, and Laurie McNeill have all given valuable advice and direction throughout the course of my research. Thank you also to Alan Taylor who helped me in the shop with jobs I wasn't competent to do for myself, and to my coworkers Wade Goodridge, Tyler Allen, and Brian Crookston who have provided valuable help in a variety of ways. Furthermore, portions of this work were made possible by the Utah State University Center for High Precision Computing, who provided computational resources.

Most of all thank you to my wife, who has patiently waited to get on with life, and to my two children who always give me a reason to smile. Their support has meant the most.

Ryan T. Christensen

CONTENTS

LIST OF TABLES

LIST OF FIGURES

CHAPTER I

INTRODUCTION

General Information

The United States has nearly 52,000 community water systems which supply water to over 292 million people (USEPA 2008). In all, nearly one million miles of pipe have been laid in order to transport water with some pipes that were installed in the 19th century still in use today (NRC 2006). Water distribution networks are a vital part of the infrastructure that society uses every day, often without a second thought. However, as pipes age, corrosion, deposition, and accretion can lead to changes in the internal surface profile of distribution system pipes. In extreme cases, the interior surface profile of an aged pipe can significantly change. Figure 1 is a photograph of the interior wall boundary of a 4-in cast iron pipe tested during this study. The pipe was used to transport culinary water for an estimated 50 years and illustrates how tuberculation (irregular buildup of corrosion byproducts) can change the surface profile of an aged pipe. Changes in the surface profile increase headloss due to friction and cause flow separation, leading to decreased flow capacity. Time dependent changes in the surface profile also add uncertainty in modeling the hydraulics of aged pipes in distribution systems.

Water distribution networks are complex systems made up of pipes, valves, storage tanks, and pumps. Due to the complexity of water distribution networks, it can be difficult to predict network response to varying demand scenarios. Accordingly,

Figure 1: Photograph inside of a 4-inch cast iron pipe tested for this study

network models have become valuable tools in understanding the day to day and extreme event operations of pipe networks and for projecting network response to changing scenarios. In recent years there has been rapid growth in the use of network models. Currently, network models are being used for a wide range of applications, from city planning to fire flow calculation and water quality modeling.

Distribution modeling has been in use for a long time, but in many ways is still a work in progress. More is being asked of today's network models than ever before and one of the greatest challenges in developing an acceptable distribution model is in the acquisition of accurate data with which to characterize the distribution system. Flow distribution, nodal heads, and the physical properties of distribution components must all be accurately described in order to develop an accurate network model. The proliferation of modern data management and gathering tools such as geographic

information systems (GIS) and supervisory control and data acquisition (SCADA) systems has helped enormously in characterizing networks. Today's network modelers often have access to more and better data than in the past; still, many of the changes that occur in aging water distribution systems are time dependent, giving rise to further complication. Pipe roughness and inside diameter are two pipe properties that may change as pipes age. Age related changes in pipe roughness can have a large effect on the capacity and headloss of a distribution system, and have received significant attention from researchers (cf. Colebrook and White 1937a, b; Williams and Hazen 1960). Diameter changes, on the other hand have been largely ignored until more recently (Boxall et al. 2004; Walski 2004). Tuberculation in aged pipes leads to a combination of increased roughness and reduced pipe diameter. Increased roughness leads to increased headloss, and reduced pipe diameter leads to increased velocities (which also increased headloss). In general modelers have preferred to adjust only roughness coefficients when calibrating a numerical distribution system model and have not addressed potential changes in pipe diameter. While this approach has been found satisfactory for calculating nodal heads, correct pipe diameters are necessary to correctly model water velocity. Furthermore, water age is dependent on water velocity. Clearly, in order to accurately model the water quality of a distribution system that contains aged pipes the reduction of pipe diameter should be considered.

Water distribution network models are based on relatively simple one-dimensional flow equations. As distribution systems may contain thousands or even

tens of thousands of pipes, this significant reduction in model complexity is necessary, and still provides good results in computing nodal heads and flow distribution. Inherently different from network modeling, computational fluids dynamics (CFD) modeling is an additional type of modeling that was applied in this study. The CFD modeling uses the three-dimensional Navier-Stokes equations for flow. Consequently, the computational requirements of CFD are much too high to be feasible for modeling an entire pipe network. Instead, CFD is particularly useful as an aid in understanding mechanisms that occur at a small scale but require a high degree of resolution. The ability to describe complex three-dimensional flows in pipes with irregular boundaries is essential for describing the mechanics of many flow processes. Examples include: the transport of dissolved materials, disinfection byproduct formation in culinary water transmission pipes, the mechanics of suspended particle accretion and subsequent erosion, and fluid mixing. Many of these processes are not fully understood in aged pipes and CFD has potential to provide new insight.

The numerical modeling of fluid flow dates back almost to the birth of modern computers. Perhaps because of their widespread use in engineering applications, pipes have been a prominent part of CFD research. However, despite the real world and academic worth, very little research has been performed with respect to aged pipes having three-dimensionally irregular boundaries. Indeed, this research appears to be the first application of CFD to a pipe with an irregular boundary surface. Two categories of CFD modeling have been included in this study. The first category is based on the

Reynolds averaged Navier-Stokes (RANS) equations. The included RANS models offer the benefits of being relatively inexpensive computationally along with being straightforward in implementation. One weakness of the RANS formulations is that they are steady state models and as a result cannot resolve the time-dependent turbulent fluctuations of flow. The second category of CFD models considered is large eddy simulation (LES). LES is an unsteady modeling technique where the smallest eddies are modeled using a subgrid-scale model, while the largest eddies are computed directly using the Navier-Stokes equations. LES is much more computationally intensive than RANS (and therefore more expensive to perform) but has the ability to model the turbulent fluctuations of flow. As this is the first application of CFD to three-dimensionally rough surfaces, the primary objective of the CFD modeling is to determine how well the two types of CFD models are able to accurately compute flow over the irregular surfaces of aged pipes.

Distribution network models and CFD each possess different sets of strengths and weaknesses. Nevertheless, the two types of modeling can be used in a complimentary manner. For example, network models are useful for calculating the nodal heads and flow rates of individual pipes within networks. CFD can then be performed, at the flow rates calculated by the network model, to provide more detailed information about the flow within a particular pipe. In this manner, the strengths of each type of model can be utilized to obtain more complete information than can be obtained by either model individually.

Dissertation Outline

The overall purpose of this study is to enable better accuracy in modeling the hydraulics of water distribution networks. The findings of this research are especially applicable to the modeling of distribution water quality. In order to achieve this purpose, five contributing objectives were identified:

1. Evaluate the changes that occur in aged pipes with respect to hydraulic roughness and flow area
2. Assess the capability of CFD for modeling the complex flow of pipes with irregular three-dimensional boundaries
3. Evaluate how the changes in aged pipes found for Objective 1 affect the hydraulics within a pipe network
    a. Macro-scale (distribution wide)
    b. Micro-scale (< 1-m)
4. Develop a method for predicting the effective diameter of a pipe based on its roughness and original diameter
5. Determine the effects of aging on distribution system performance using a simplified model of an existing network

The following paragraphs outline the individual chapters of this dissertation and describe how the contents of each chapter contribute toward meeting the project objectives.

The purpose of Chapter II is to present background information pertinent to Chapters III through V that is not contained elsewhere in this report. Specifically, Chapter II summarizes the physical testing of the eleven aged pipes obtained for this study. Each pipe was subjected to laboratory testing to quantify the age related changes that had occurred in the pipes with respect to hydraulic roughness and flow area. The pipe sections varied in age from 25 to 50 years and in nominal diameter from 0.020-m (0.75-in) to 0.100-m (4-in). In general, L/D for the pipes varied between 20 and 40 where L represents pipe length and D represents pipe diameter. Of the aged pipes tested, area reduction was found to be as high as 23%. Hazen Williams C of the aged pipes was highly variable with an approximate range of 40 to 145 depending on pipe condition. Also specified in Chapter II are the pipes tested using CFD modeling. Two pipes with nominal diameters of 0.025-m (1-in) and 0.050-m (2-in) were modeled using RANS turbulence modeling and one pipe with a nominal diameter of 0.050-m (2-in) was modeled using LES. The background information in Chapter II also helps address Objective 1.

Chapter III demonstrates the application of the laboratory test data in calibrating a model pipe network that contains aged pipes. In order to apply the laboratory findings to the model network, a method for estimating the effective diameters of aged pipes was developed based on the laboratory findings and using a manipulation of the Hazen-Williams equation. The importance of using correct pipe diameters is illustrated by comparing two scenarios. In the first scenario only friction coefficients are reduced

in order to compensate for the increased headloss of aged pipes. In the second scenario diameter reduction is also considered. Both networks were modeled using EPANET 2 (USEPA 2000). Comparison of the two networks demonstrates the magnitudes and types of errors that can be introduced by ignoring possible changes in the flow area of aged pipes. In particular, reducing the pipe diameters of aged pipes was found to reduce the age of water within the sample distribution system by up to 10% and was found to significantly impact the variation in water age that occurs as a result of fluctuations in daily demand. Objectives 3.a, 4, and 5 are all addressed by Chapter III.

In Chapter IV the Reynolds-Averaged Navier-Stokes (RANS) equations for three-dimensional flow are solved to compute flow through two of the aged pipes that previously underwent laboratory testing. Flow in a 0.025-m (1-in) pipe is solved at a Reynolds number of 13,000, and a 0.050-m (2-in) pipe is solved at Reynolds numbers of 6700 and 31,000. Three turbulence models were applied to each flow scenario including a 4-equation $v^2 - f$ model, and 2-equation realizable $k - \varepsilon$ and $k - \omega$ models. The RANS turbulence models calculated headloss directly based on the flow in the rough pipe. The calculated headloss was then used to determine a friction factor for each model and flow scenario, which was then compared against the laboratory results. The $v^2 - f$ model was the most accurate model for replicating the laboratory measured friction factors, giving values that ranged from 5% higher to 15% lower. Velocity profiles are also presented, giving a demonstration of the detailed flow information that can be

obtained via RANS turbulence modeling. Chapter IV directly addresses Objectives 2 and 3.b.

In Chapter V the filtered Navier-Stokes equations are solved to perform large eddy simulation (LES) on a 0.050-m (2-in) pipe at a Reynolds number of 6800. Similar to the RANS turbulence modeling, the headloss computed by the LES was used to determine a corresponding friction factor for comparison against the laboratory results. The LES produced Darcy-Weisbach friction factors were 20% lower than the friction factors obtained via experimental testing. While Chapter V also addresses Objectives 2 and 3.b (the same objective addressed by Chapter IV), the purpose for including LES is to demonstrate the ability of LES to resolve the turbulent fluctuations of flow. This added capability is necessary for understanding flow processes that are dependent on turbulence. Profiles of velocity and root-mean-square velocity fluctuations were presented, demonstrating the detailed information obtainable via LES.

Properly applied, the information presented in this study will improve the modeling of water quality (and perhaps other processes) within water distribution systems. The depiction of the changes in flow that may occur in aged pipes along with the groundbreaking applications of CFD to three-dimensionally irregular surfaces add to the list of study contributions as summarized below.

1. The effect of aging pipes on distribution hydraulics has been outlined with respect to modeling correct water age
2. A method for correcting the diameters of aged pipes has been described

3. CFD has been used to compute flow in an aged pipe for the first time
    a. RANS
    b. LES
4. CFD has been demonstrated to be a useful method for describing flow over small (≈1-m or less) sections of three-dimensionally irregular pipes

While network distribution models and CFD models are used for seemingly dissimilar applications and provide different types of results, the two categories of models can be used in a complimentary manner. Network modeling can provide the nodal heads and flow distribution within a pipe network. Using the flow rates from a network model, CFD can then be used to improve the understanding of the basic mechanics of the processes that occur as flow moves through an aged pipe. Furthermore, improving the understanding of the basic mechanics of flow processes will enable the development of more descriptive models.

CHAPTER II

BACKGROUND

Laboratory Testing

Much research has been conducted with respect to the effects of aging pipes on water transmission (cf. Colebrook and White 1937a, b; Williams and Hazen 1960; Mamrelli and Streicher 1962; Sharp and Walski 1988; Boxall et al. 2004). The accumulation of material on the inside wall of distribution pipes has two primary effects: increased roughness and reduced pipe diameter (Colebrook 1937a). However, as noted previously, most attention has been given to the changes that occur in roughness, while very little consideration has been given to changes in pipe diameter. In order to address this deficiency, eleven aged pipes were located, obtained, and subjected to laboratory testing. The pipe sections varied in age from 25 to 50 years and in nominal diameter from 0.020-m (0.75-in) to 0.100-m (4-in). In general L/D for the pipes varied between 20 and 40 where L represents pipe length and D represents pipe diameter. The internal volume of each pipe section was determined by filling the pipe sections with water and measuring the water volume. Effective pipe diameter was then back-calculated by manipulating the equation for the volume of a cylinder ($\not{V} = \pi \cdot d^2/4 \cdot L$) to solve for effective diameter where $\not{V}$ is the volume of a cylinder, d is the effective diameter, and L is the pipe length. Thus, the effective diameter represents the diameter of a smooth cylinder that will have the same length and volume as the pipe test section. The diameter ratio, d/D, was calculated by dividing this calculated effective

diameter (d) by the inside pipe diameter (D) as obtained from a table of standard pipe diameters for new pipe (ASME 2004). The results are tabulated in Table 1 and facilitate assessment of the degree to which the internal diameter of the aged pipes changed as a result of tuberculation. Furthermore, because of insufficient age data no effort has been made in this study to use age as a determining factor in estimating pipe roughness.

In addition to the volumetric measurements, hydraulic roughness testing was also performed. The hydraulic testing was performed by installing each aged pipe in a laboratory test line and measuring the headloss at multiple flow rates. The measured

Table 1: Summary of Aged Pipes

Pipe Section	Pipe Description	D-meters (in)	d-meters (in)	d/D
1	galvanized steel	2.093E-2 (0.824)	1.949E-2 (0.767)	0.931
2	galvanized steel	2.093E-2 (0.824)	1.974E-2 (0.777)	0.943
3	galvanized steel	2.093E-2 (0.824)	1.985E-2 (0.781)	0.948
4	galvanized steel	2.664E-2 (1.049)	2.334E-2 (0.919)	0.876
5	galvanized steel	2.664E-2 (1.049)	2.434E-2 (0.958)	0.914
6	galvanized steel	5.251E-2 (2.067)	5.005E-2 (1.970)	0.953
7	thin-walled steel	9.738E-2 (3.834)	9.483E-2 (3.733)	0.974
8	bituminous coal lined cast iron	1.023E-1 (4.026)	9.407E-2 (3.703)	0.920
9	bituminous coal lined cast iron	1.023E-1 (4.026)	1.020E-2 (4.017)	0.998
10	bituminous coal lined cast iron	1.023E-1 (4.026)	1.021E-2 (4.022)	0.999
11	bituminous coal lined cast iron	1.023E-1 (4.026)	1.023E-1 (4.026)	1.00

values of headloss and flow rate were then used to calculate Hazen-Williams C values for each pipe using the Hazen-Williams equation (Equation 1).

$$v = kC\left(\frac{D}{4}\right)^{0.63} S^{0.54} \quad (1)$$

where v, C, and D are the velocity, Hazen-Williams coefficient, and the pipe diameter; k is a constant that depends on units (1.318 for US customary units), and S is the slope of the energy grade line (friction slope). In addition, friction factors were computed using the Darcy-Weisbach equation (Equation 2)

$$h_f = \frac{v^2}{2g}\frac{f \cdot L}{D} \quad (2)$$

where h_f is the headloss due to friction, f is the Darcy-Weisbach friction factor, and g is the acceleration due to gravity with other variables as previously define. Figure 2 is a plot of Hazen-Williams C versus Reynolds number obtained from the headloss testing with the pipes labeled according to Table 1. A chart similar to Figure 2 but using the Darcy-Weisbach friction factor in place of Hazen-Williams C has been included as Figure 30 in the Appendix. Confidence intervals have been included for the roughness coefficients in Figures 2 and 30. All confidence intervals were calculated by performing a root-mean-square error analysis using error progression based on the maximum expected errors for each laboratory measured quantity.

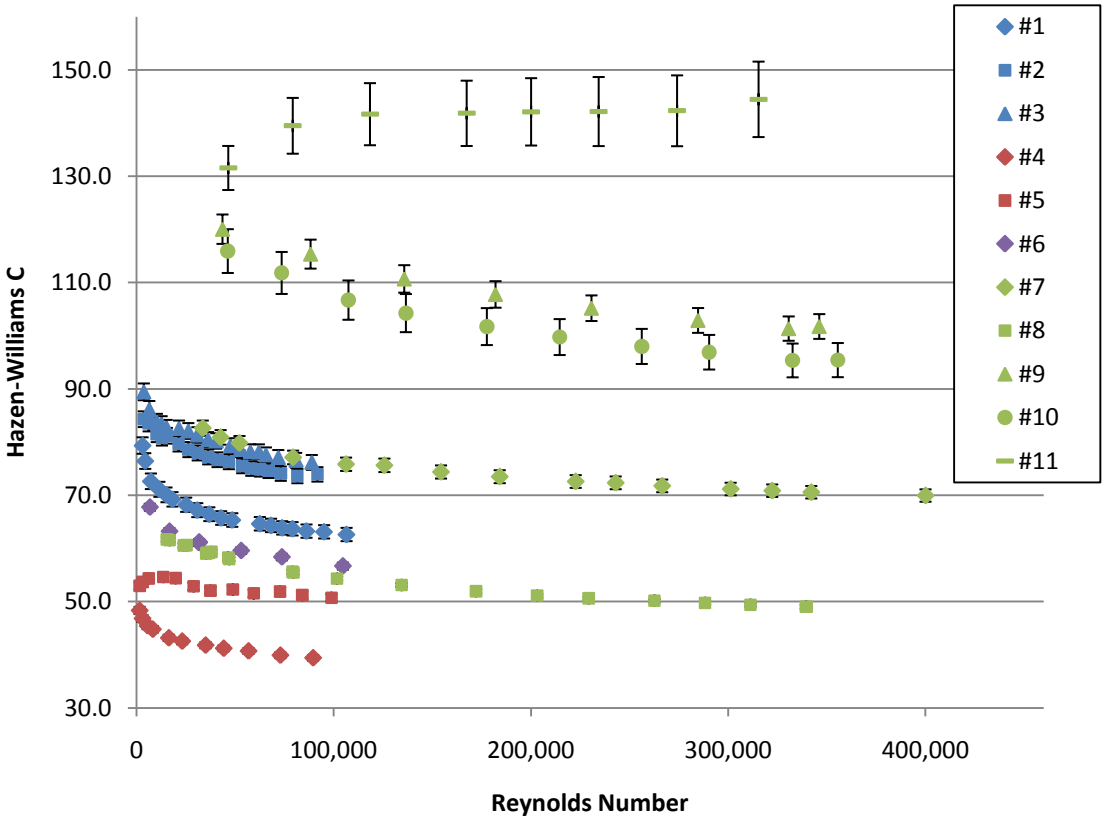

Figure 2: Plot of Hazen-Williams C versus Reynolds number with confidence intervals

The determination of which roughness coefficient (Hazen-Williams C or Darcy-Weisbach friction factor) to use for a specific chapter within this report was based on the intended application and audience. Chapters III, IV, and V have been written as technical papers. Chapter III is written for an audience with expertise in the field of water distribution network modeling and Hazen-Williams C has been used extensively throughout that chapter. On the other hand, Chapters IV and V are written for an audience with expertise in computational fluid dynamics modeling and as a result make use of the Darcy-Weisbach friction factor.

CFD Modeling

CFD modeling was also performed on pipes 5 and 6 (cf. Table 1) with nominal diameters of 0.025-m (1-in) and 0.050-m (2-in), respectively, using the general purpose CFD code FLUENT (Fluent 2006). The two pipes were physically split longitudinally to facilitate high resolution laser scanning of the internal pipe wall in order to obtain accurate three-dimensional representations of the internal wall profiles of each pipe. After scanning, the digital halves of each pipe were recombined and used to specify the wall boundary conditions in performing CFD modeling. Each of the digitized pipes was modeled using turbulence models based on the Reynolds averaged Navier-Stokes (RANS) equations for three-dimensional fluid flow. The 0.025-m (1-in) pipe was tested at a Reynolds number of 13,000 while the 0.050-m (2-in) pipe was tested at Reynolds numbers of 6700 and 31,000. Each flow condition was chosen to match a specific laboratory test run to facilitate straightforward comparisons between laboratory and CFD results. The basic steps in the RANS modeling included building a computational mesh, developing and specifying boundary conditions, and iterating to achieve convergence. Detailed explanation of each step is included in Chapter IV. The steps in performing the large eddy simulation (LES) were very similar to those outlined for RANS. However, LES is much more computationally intensive than RANS. As a result, the LES portion of this study was comprised of a single simulation using the 0.050-m pipe at a Reynolds number of 6800. Chapter V details the steps involved in performing the LES.

CHAPTER III

IMPROVING WATER QUALITY MODELING IN SYSTEMS CONTAINING TUBERCULATED PIPES[1]

Abstract

Laboratory testing was performed on aged pipes with varying degrees of turberculation in order to characterize the relationship between reduced pipe diameter and Hazen-Williams C. These results, combined with a manipulation of the Hazen-Williams equation, provided a simple and direct method for addressing potential changes in pipe diameter. This method was then applied to a network model using EPANET 2. The network modeling application demonstrates the magnitudes and types of errors that can be introduced to water age in a network model by ignoring possible changes in the flow area of aged pipes. Specifically, it was found that the largest error introduced was in the pattern of fluctuations that occurs as different source waters moved through the distribution system.

Introduction

Water distribution networks are complex systems made up of pipes, valves, storage tanks, and pumps - along with many other parts. Due to the complexity of water distribution networks, it is very difficult to comprehend their operation just by reviewing a network schematic. Network models have become a valuable tool in

[1] Coauthored by Ryan T. Christensen, Steven L. Barfuss, P.E., and Michael C. Johnson, Ph.D., P.E.

understanding the day to day and extreme event operations of networks and for investigating the response of a network to various scenarios. In recent years there has been rapid growth in the usage of network models; still, there are several difficulties faced in developing accurate models. One of the most significant difficulties is the acquisition of adequate data (e.g. nodal heads, flow distribution, pipe characteristics, etc.) in order to accurately characterize pipe networks. This challenge arises as a result of incomplete records, undocumented changes, and because pipe properties such as roughness and flow area may change as certain types of pipes age. The degree to which age based degradation occurs is highly dependent on water quality, pipe material, and the type of coating applied to a pipe (Colebrook and White 1937a; Williams and Hazen 1960; Lamont 1981; Sharp and Walski 1988). The reconciliation of inaccurate network data is generally accomplished through a process of calibration whereby physical data (such as nodal head values) are measured within a network and compared to simulated values obtained from a network model. By comparing the measured values to the simulated values and adjusting the physical attributes of the network model it is possible to improve the correlation between the network model and the actual network by identifying and rectifying inconsistencies in the network model. Throughout this process, it is of vital importance to ensure that any changes made to the input parameters of a distribution network are justifiable based on the supporting evidence (Hirrel 2008).

While developing an accurate hydraulic model is a necessary part of modeling water quality, network models that will be used to model water quality have special requirements versus those that will only be used to model hydraulic conditions. Network models that focus on modeling hydraulics are commonly calibrated by comparing the nodal heads within the hydraulic model to heads measured in the pipe network and adjusting the friction coefficients of pipes within the network so that the modeled and measured values are within an acceptable tolerance of error. During this process, potential changes in pipe diameter are normally given little consideration (Boxall et al. 2004; Walski 2004). Although this method is usually satisfactory for situations in which a model will be used for simulating pressures and fire flows, this procedure does not account for possible changes in flow area resulting from pipe age and as a result may not model the appropriate water velocities needed for the accurate modeling of water age. Moreover, many water quality problems including disinfectant decay, disinfection by-product formation, and taste and odor problems have been associated with the residence time of water in distribution systems (AWWA and EES 2002). Research by Hallam et al. (2002) and Clark and Haught (2005) has also indicated that chlorine decay rate is a function of velocity. While this research is not commonly applied in the current network models, future models may account for this dependence which would further reinforce the importance of accurately modeling water velocity. In order to address these issues, several studies have suggested the need to adjust the

diameter of aged pipes that have significantly reduced flow areas when modeling water quality (Skipworth et al. 2002; AwwaRF 2004; Boxall et al. 2004; AWWA 2005).

For example, Boxall et al. (2004) recommended the assumption that a 1-mm effective roughness height is equal to a 2-mm loss in diameter. While this approach may be accurate in some cases, it is important to remember that the early tests upon which the idea of effective roughness height is based were performed using sand grains as the roughness elements (Nikuradse 1933; Prandtl 1933; Colebrook and White 1937b). As a result, other types of roughness elements may not have a direct physical correlation with effective roughness height. Still, a correlation between roughness and area reduction would be very useful for aged pipes. However, such a correlation cannot be obtained from roughness testing performed on arbitrary surfaces, but instead requires the testing of actual aged pipes.

Interest in water quality modeling is increasing. One portion of a 1999 survey commissioned by the AWWA Engineering and Computer Applications Committee sought to determine current and planned applications for water quality modeling (AWWA 2005). Among the applications cited by survey respondents were: replacing water quality monitoring with modeling, obtaining operational information, investigation of water age, and locating and sizing storage tanks. Growth in the field of water quality modeling is expected to continue. However, the potential changes that can occur in aged pipes continue to be a challenge in developing accurate network models, especially with respect to accurately modeling water age. The objective of this paper is

to provide guidance that will enable system modelers to improve their estimates of water age in networks with degraded pipes. Laboratory testing has been used to assess the changes that occur in aged pipes. The laboratory test results are presented and the effects of these changes on modeling water age were explored by applying the findings of the laboratory testing to a pipe network.

Laboratory Testing

Laboratory testing was conducted in order to evaluate the hydraulic and physical characteristics of sections of aged pipe. The primary objective of the physical testing was to investigate methods for estimating the amount of area reduction and to determine the amount of headloss present in the aged pipes. Eleven aged pipe sections were obtained from water utilities and subjected to physical testing. The pipe sections varied in age from 25 to 50 years and in nominal diameter from 0.75-in to 4-in. The majority of the pipe sections varied in length from 20 to 40 pipe diameters. Most were acquired when utilities were repairing or replacing a pipe section. Testing was performed in order to determine an effective diameter and to evaluate the roughness of each pipe section. For this purpose, the internal volume of each pipe section was determined by filling the pipe sections with water and then measuring the volume of the water. An average pipe diameter was then back calculated using the volume of the water and the pipe length with the assumption of a circular pipe cross section. The diameter ratio, d/D, was obtained by dividing this calculated average diameter (d) by the inside pipe diameter (D) in its new condition as obtained from a table of standard

pipe diameters for new pipe (ASME 2004). The standard pipe diameter was used because it is generally easy to obtain and in many cases represents the best available estimate for the original pipe diameter that would be available to a distribution system modeler. Table 2 provides a summary of the aged pipe sections tested during this study. A d/D value of 0.95 indicates that a pipe's diameter has been reduced by 5%. Because the velocity for a given flow rate is inversely proportional to the square of pipe diameter, a 5% reduction in diameter will result in an increase of 10.8% in velocity for

Table 2: Description of Aged Pipes

Pipe Section	Pipe Description	D (in)	d (in)	d/D	Percent Reduction in Flow Area
1	galvanized steel	0.824	0.767	0.931	13
2	galvanized steel	0.824	0.777	0.943	11
3	galvanized steel	0.824	0.781	0.948	10
4	galvanized steel	1.049	0.919	0.876	23
5	galvanized steel	1.049	0.958	0.914	16
6	galvanized steel	2.067	1.970	0.953	9.2
7	thin-walled steel	3.834	3.733	0.974	5.1
8	bituminous coal lined cast iron	4.026	3.703	0.920	15
9	bituminous coal lined cast iron	4.026	4.017	0.998	0.40
10	bituminous coal lined cast iron	4.026	4.022	0.999	0.20
11	bituminous coal lined cast iron	4.026	4.026	1.00	0

that flow rate. Thus, changes that occur in pipe diameter result in comparatively larger changes in velocity. Based on the physical testing performed during this research, the pipe sample with the largest reduction in flow area was estimated to have lost 23% of its area as compared to a new pipe. Modeling this pipe without accounting for changes in flow area would result in modeled flow velocities being 23% lower than actual velocities. Three of the pipes that were tested during this study had flow area reductions of less than 1% while the remaining seven lost between 5.1% and 16% of their new pipe flow area.

After determining the effective diameter, hydraulic roughness testing was performed. The hydraulic testing was carried out by installing each aged pipe section in a laboratory test line and establishing a constant flow rate through the pipe. The headloss due to friction across the pipe and the flow rate were measure. The measured values of headloss and flow rate were then used to calculate a Hazen-Williams C (based on the effective pipe diameter d) for each pipe. Figure 3 is a plot of the relationship found between d/D and Hazen-Williams C for the eleven pipes (for a similar plot in terms of the Darcy-Weisbach friction factor refer to Figure 31 in the Appendix). It can be seen that as the d/D ratio decreases the roughness of the pipes increases. Initially, from the pipe's new condition with d/D = 1, Hazen-Williams C drops rapidly compared to small decreases in d/D. However, below d/D = 0.97 the relationship has a much milder slope. A trend line has been added over the mild portion of the curve for d/D < 0.97; however, this is a preliminary trend line included for convenience in this work. As

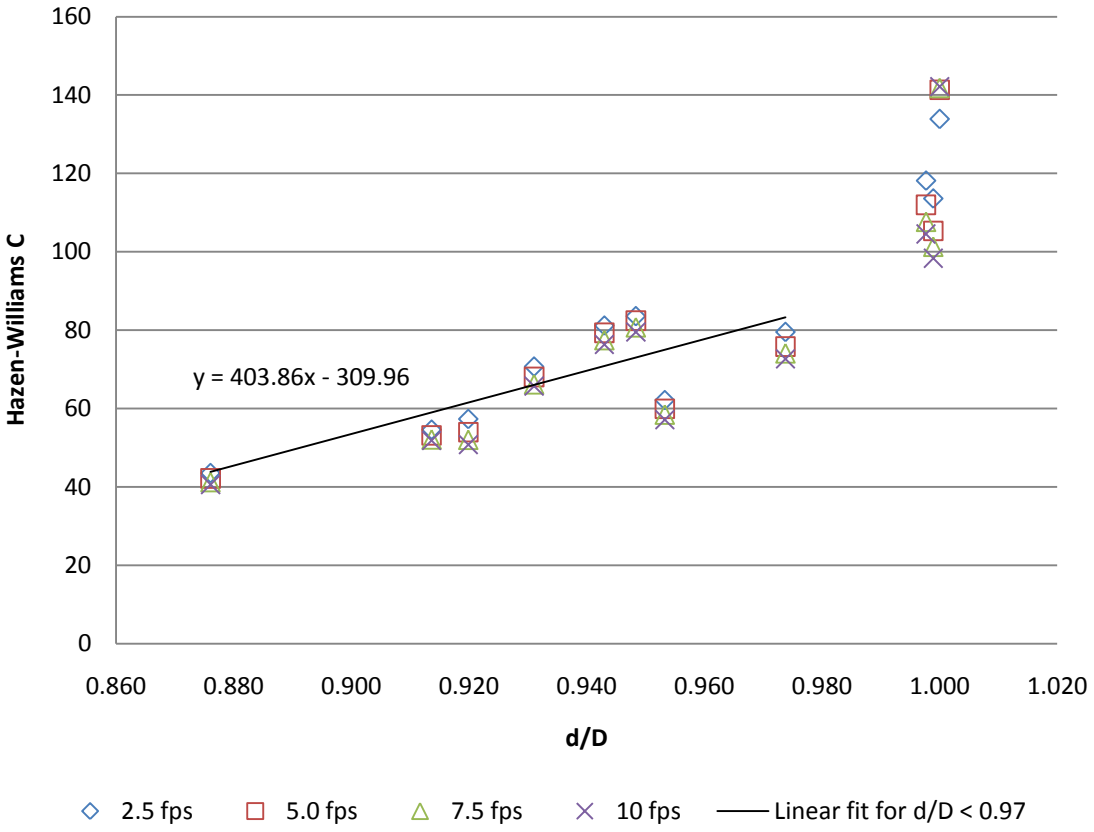

Figure 3: Plot of d/D versus Hazen-Williams C

a result, caution should be exercised in its general application to aged pipes. Each cluster of points in Figure 3 represents testing on a single pipe section at multiple flow velocities. Results for different velocities have been included so that the reader is aware of the changes observed in Hazen-Williams C as a function of velocity. Specifically, the dependence of the Hazen-Williams C factor on velocity is less for cases where the Hazen-Williams C is below 90 as opposed to the cases where C is greater than 90. Also, it is important to note that many of the pipe sections tested during this study were chosen because they showed visible signs of age related degradation. Accordingly, this subset of pipes is not expected to be generally representative of the roughness of pipes

in distribution networks but rather is used to illustrate the relationship between pipe roughness and diameter reduction.

Pipe Network Application

Network demonstration. In order to show the effects of area reduction on the accuracy of a pipe network model, the results of the physical tests were applied to an example pipe network using EPANET 2 (USEPA 2000). The objective of the pipe network application is to demonstrate how the relationship between d/D and C factor can be applied during the calibration of a network model. In order to accomplish this, the sample network was first modeled with very low C factors but without addressing potential changes in pipe diameter. Next, pipe diameter changes were addressed according to the results presented in Figure 3 and the modeling of the sample network was repeated. The results obtained from each model were compared in order to assess the importance of adjusting pipe diameters. In order to differentiate between the two networks, Case 1 will refer to the condition where only C factors were reduced and Case 2 will refer to the condition where diameter and C factor were both adjusted. The following sections provide background information regarding the sample network, describe how C factors were reduced for Case 1, and present the process used in reducing pipe diameters to obtain the network for Case 2.

Sample pipe network. The sample network is a hydraulically isolated portion of an actual network. The network has one reservoir, one storage tank, one pressure

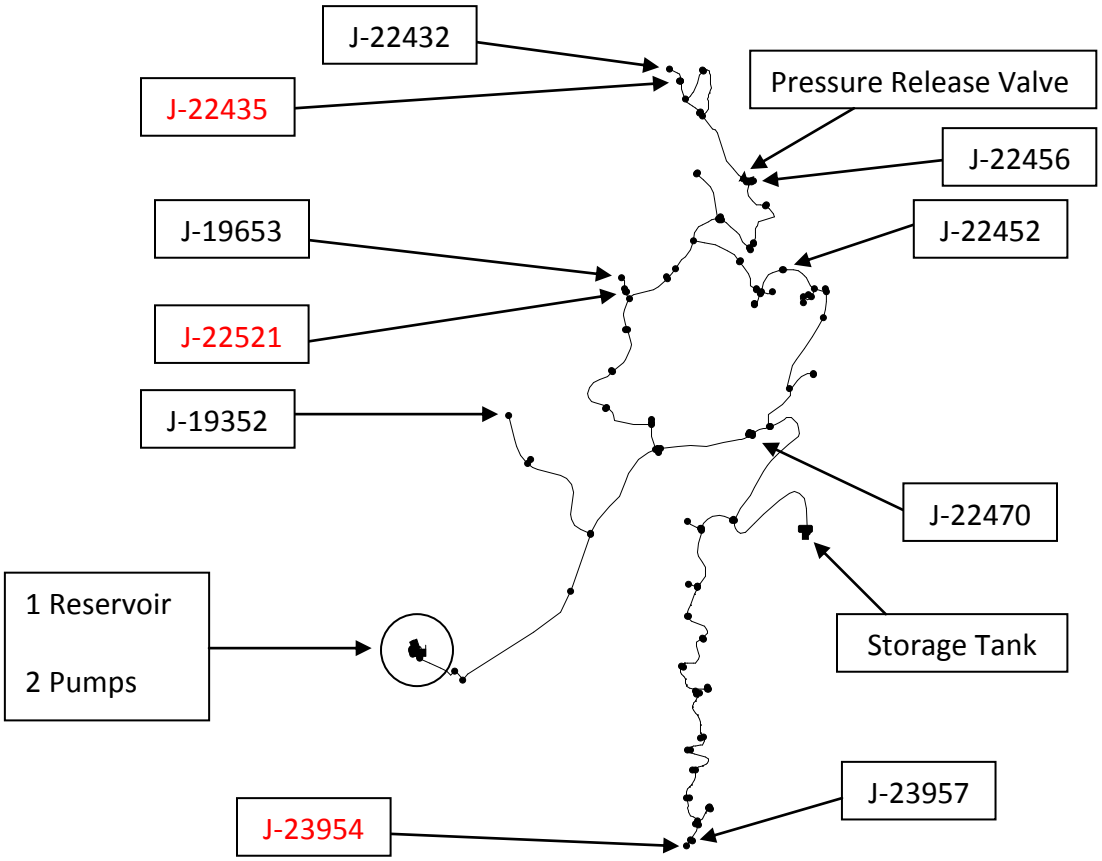

Figure 4: Network model utilized for simulations – red indicates junctions where hydrant demands were simulated, black junctions represent monitoring locations

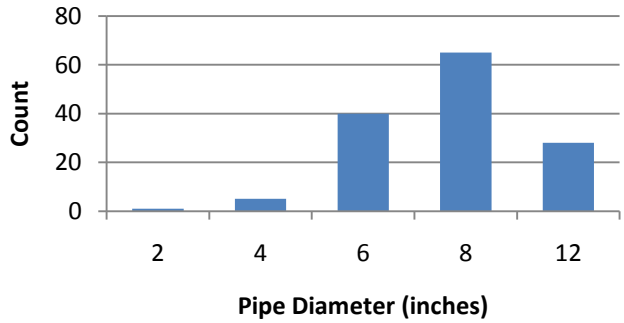

Figure 5: Pipe size distribution for the sample network

release valve, and two pumps as shown in Figure 4. The sample network has 137 nodes and 139 pipes with a size distribution as shown in Figure 5.

Case 1: reduce C factors. When new, the pipes in the sample network would be expected to have C factors in the range of C = 130 - 140. However, in order to simulate severe age degradation the C factor of each pipe in the sample network was reduced to 65. A C factor of 65 is roughly centered along the trend line in Figure 3 for d/D < 0.97. While using the same C factor for every pipe is a simplification in that small pipes generally show more pronounced age related degradation than large pipes (Williams and Hazen 1960), this assumption does not affect the validity of the procedure presented in this analysis. The sample network with reduced C factors represents an aged network that has been calibrated using nodal heads without consideration for any changes in diameter that may have occurred during the aging process.

Two types of network simulations were then run on the aged network. First, fire hydrant testing was simulated. The hydrant simulations consisted of three hours of regular operation followed by one hour with a 250 gpm hydrant test, one hour at 500 gpm, and one hour at 750 gpm followed by four hours of regular operation. This process was repeated at three different locations in order to ensure that there was at least one run for each of the seven monitoring nodes that produced sufficient headloss in order to adequately assess calibration. Next, extended period simulations were performed under conditions simulating normal daily operations.

Case 2: adjust pipe diameters. The network with reduced C factors was modified in order to consider diameter reduction. The development of the method used in

estimating reduced pipe diameters is detailed below and concludes with a short example.

The Hazen-Williams equation can be written as

$$v = kC\left(\frac{D}{4}\right)^{0.63} S^{0.54} \tag{3}$$

where v, C, and D are the velocity (ft/s), Hazen-Williams coefficient, and the pipe diameter (ft); k is a constant that depends on units, and S is the slope of the energy grade line (friction slope). Rewriting Equation 3 in terms of flow and defining a new constant k' (about 0.432 when length and flow are measured in feet and cfs respectively) for all of the constants gives Equation 4.

$$Q = k'CD^{2.63}S^{0.54} \tag{4}$$

Calibration data provide a description of the relationship between the flow rate Q (cfs) and the slope of the energy grade line (S). However, because of potential changes in pipe diameter there are still two unknowns in Equation 4: diameter and C factor. One of the easiest ways to address this problem is to simply assume that pipe diameters are unchanged which then allows direct computation of C factor. However, employing this method has the aforementioned disadvantage of modeling incorrect velocities. Equation 4 may be rewritten in terms of an unknown aged pipe diameter as shown:

$$Q = k' C_d d^{2.63} S^{0.54} \quad (5)$$

where C_d is the Hazen-Williams C based on a reduced diameter and d is the reduced diameter. Equation 5 can be set equal to Equation 4 and the ensuing simplifications lead to

$$\frac{C}{C_d} = \left(\frac{d}{D}\right)^{2.63} \quad (6)$$

The most important observation from Equation 6 is that for any known values of C and D, an infinite number of corresponding pairs of C_d and d exist that will result in an identical relationship between flow rate and energy slope as the original C and D. While Equation 6 is interesting on an academic level, its practical value is limited. While there are an infinite number of pairs that provide the proper relationship between flow rate and headloss, only one pair results in the correct velocity for a given pipe and the arbitrary selection of that correct pair is problematic without additional information. The additional information is provided by the trend shown in Figure 3:

$$C_d = 403.86 \frac{d}{D} - 309.96 \quad (7)$$

When combined, Equations 6 and 7 allow direct solution of the correct C_d and d values based on the laboratory experiments of aged pipes. A convenient byproduct of the described formulation is that network models can first be calibrated for headloss by only changing C factors. Later, if necessary, diameter corrections can be applied

retroactively to improve the modeling of water age without affecting the original calibration for headloss. Calibration of a water distribution network would be carried out in the following manner: first, calibrate the network based solely on headloss, next review the C factors to determine if the roughness is sufficient to merit the reduction of pipe diameter, and if reductions are justified, use equations 4 and 5 to determine C_d and d for the pipes. The following example demonstrates the implementation of this method.

Example 1

Consider a case with a single pipe connecting two nodes in a network. The slope of the energy grade line (S) between the nodes is 0.00308, the flow rate (Q) is 90 gpm (0.2 cfs), and the inside diameter (D) of the pipe when new was 6-in (0.5-ft). However, the pipe has an unknown reduced diameter (d) as a result of aging. Using Equation 4 with the assumption that the new pipe diameter is applicable gives $C = 65$. However, a quick check of Figure 3 indicates that for $C = 65$ an appreciable reduction in diameter will have occurred. Next, Equation 7 is solved for d/D and substituted into equation 4 which allows easy calculation of $C_d = 74$. Either Equation 6 or 7 may then be used to determine the appropriate d/D (for this example 0.951). The last step is to multiply the value of d/D by the original pipe diameter in order to determine the reduced diameter which in this example is 5.71-in. Thus, in order to compensate for area reduction the pipe

diameter should be reduced from 6-in to 5.71-in and the C factor increased from 65 to 74.

While Example 1 is a simplified case applied to a single pipe joining two nodes, the same method can be applied to a large pipe network. Furthermore, the method formulation guaranteeing the flow rate versus headloss relationship will be unchanged by diameter changes is very beneficial. This enables a modeler to first calibrate a network model based on headloss and flow distribution and then adjust pipe diameters as necessary to improve the modeling of water age without changing the status of a model's original calibration.

Case 1 was modified to obtain Case 2 using the procedure outlined in Example 1. Fire hydrant and extended period simulations were repeated for Case 2. Comparison of the fire hydrant testing results obtained from Cases 1 and 2 provided verification that the two networks produced the same nodal heads and flow distribution. Comparison of the results from extended period simulations allowed evaluation of the importance of addressing potential changes in pipe diameter when modeling water age.

Comparison of results. The C factor and diameter reduction that were applied to the diameter reduced network were $C_d = 74$ with a d/D ratio of 0.951 (see Example 1). A d/D ratio of 0.951 corresponds to a 9.5% reduction in flow area. Figure 6 is a plot of the head at node J-23957 while simulating fire hydrant testing at node J-23954. As expected, the nodal heads in Cases 1 and 2 were found to be identical within rounding error. Furthermore, the correlation for head shown in Figure 6 was typical of the

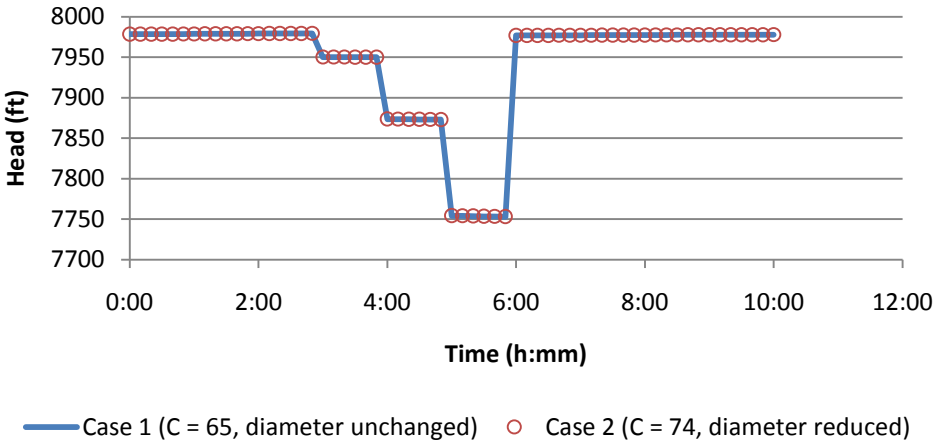

Figure 6: Head at node J-23957 while simulating fire hydrant testing at J-23954

correlation between Cases 1 and 2 for nodal heads and flow distribution for each of the monitoring nodes. This demonstrates that the application of the method outlined in Example 1 allows adjustment of pipe diameters and C factors without changing the calibration status of a network model that has already been calibrated.

After demonstrating that Case 2 maintained the same nodal heads and flow distribution as Case1, the extended period simulations were conducted in order to identify the changes that occur in water age as a result of reducing pipe diameters. Figure 7 shows a plot of water age in the storage tank. Reducing the pipe diameter led to a reduction of 6.8% in the modeled peak water age in the storage tank while reducing the minimum water age by 7.2%. Figure 8 is a plot of water age versus time at node J-22452. The relationship between water age and time shown in Figure 8 is typical of most of the monitoring nodes in the distribution system. In general, the peak water age at the monitoring nodes was decreased by 6.7-8.4% and the minimum water age was

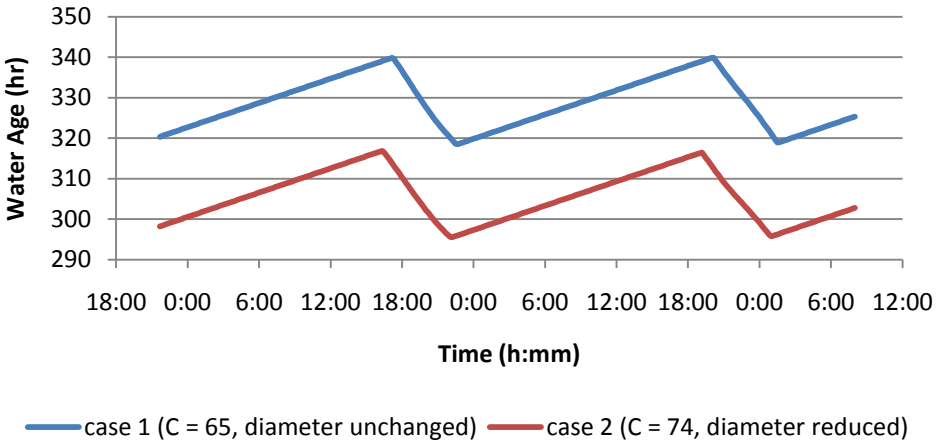

Figure 7: Water age in the storage tank

decreased by 7.4-10% (with one exception as noted in the following paragraphs). These values are reasonable considering the 9.5% reduction in flow area caused by applying the d/D ratio of 0.951. The reduction in peak water age is generally smaller than the reduction in minimum water age because of the influence of the storage tank. Reducing pipe diameters affects travel times but not the time the water spends in storage. Furthermore, it can be seen that the variable with the most impact on water age is

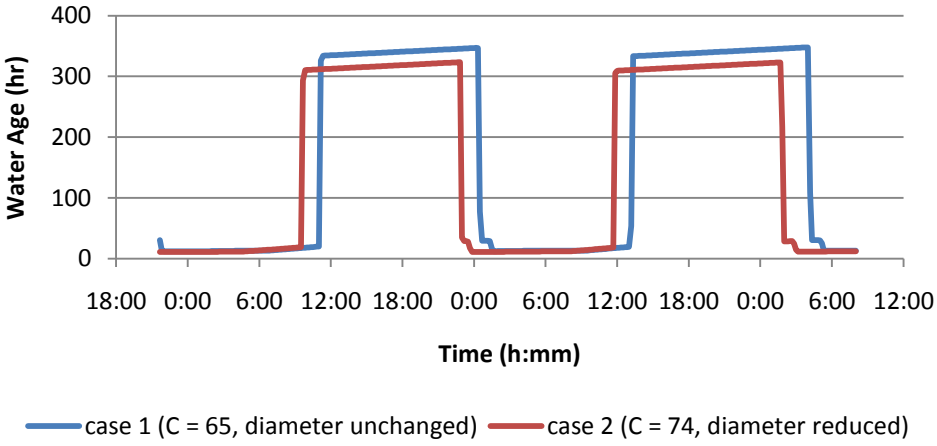

Figure 8: Water age versus time at node J-22452

water source: whether the water is coming directly from the reservoir or directly from the storage tank. In Figure 8 it can be seen that the x-axis offset between water age peaks for Case 1 and Case 2 is fairly small (~1:20). This is because the travel time from the storage tank to node J-22452 is relatively short. Figure 9 illustrates the much larger (~8:40) offset that occurs at node J-22456. Because of the longer travel time, ignoring changes in pipe diameter would have a much larger effect at node J-22456 than at node J-22452. This demonstrates that changing pipe diameters can have a large effect on the fluctuations in water age that occur due to changes in the operational status of pumps and storage tanks. The situation becomes even more complex when combining operational variables and looping pipe structures as shown in Figure 10. Due to the travel times of water originating from the reservoir and the storage tank and the mixing that occurs at various nodes, the water age versus time relationship at node J-22432 is very complex and varies significantly between the two networks. It is also notable that

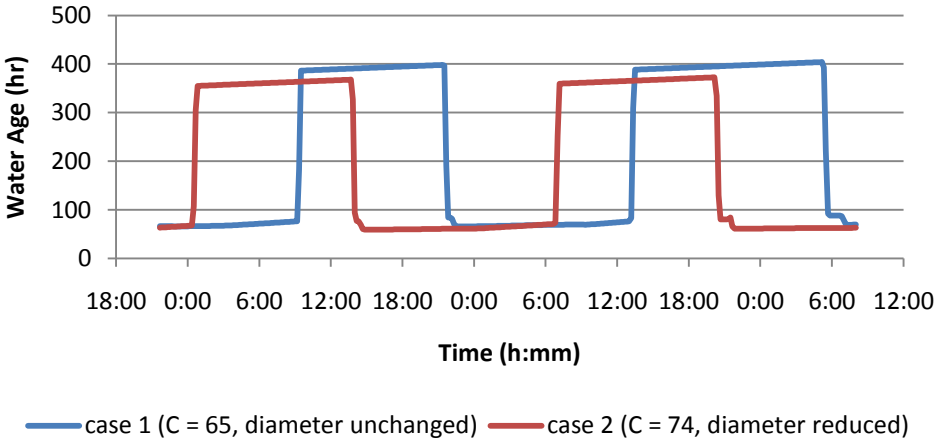

Figure 9: Water age versus time at node J-22456

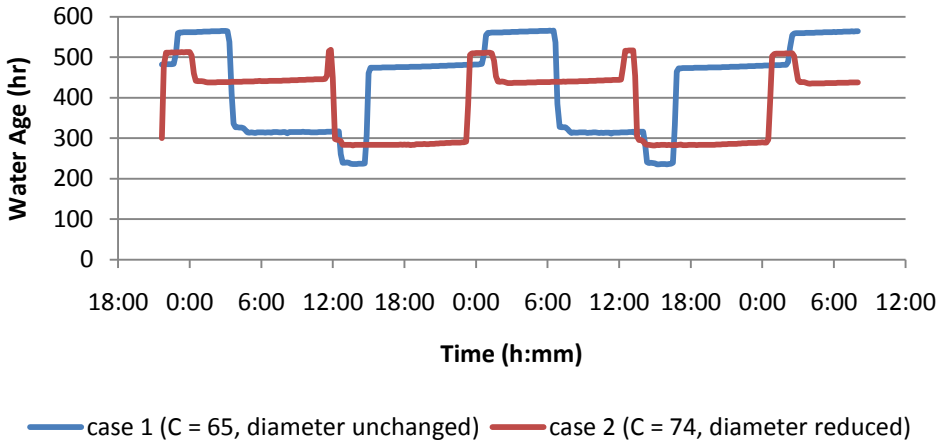

Figure 10: Water age versus time at node J-22432

this was the single monitoring node where applying diameter reductions lead to an increase in minimum water age.

In summary, two significant differences are observed in networks as a result of reducing pipe diameters to compensate for aged pipe as opposed to only reducing C factors: water age is reduced and the pattern and timing of the fluctuations that occur as a result of the changing operational status of pumps and storage tanks is altered. The largest age reductions for the sample network were observed to be about 10%. For applications where modeling the pattern of the changes in water age is crucial using the correct pipe diameter is especially critical.

Conclusions

While many researchers have noted the importance of using accurate pipe diameters for modeling water quality, this can be a very difficult task to implement in practice. This paper has presented data that quantify the degree to which diameter and

velocity changed in several aged pipes as well as outlined a process for applying these data in the calibration of pipe network models. The method of application has been shown to be useable without affecting the current calibration status of a network model that has been calibrated for nodal heads and flow distribution. Although the trend shown in Figure 3 is not expected to be descriptive of all aged pipes, it acts as a useful guideline for modelers working with aged networks. Modelers should be especially cautious when applying the trend in Figure 3 to pipes that are considerably larger than the pipes analyzed for this study. Moreover, the dominant process causing increased roughness and diameter reduction in the pipes analyzed for this study was iron corrosion. Other degradation processes (calcium scale buildup, biofilm formation, etc.) may not follow the relationship between d/D and C factor described by the trend line in Figure 3.

The pipe network application highlights some of the inaccuracies introduced by not accounting for diameter changes in pipes. First, applying the data in an example system resulted in a decrease of 6.7-8.4% in peak water age and a decrease of 7.2-10% in the minimum water age. In addition, the reductions in travel time were found to produce several interesting changes in the patterns of water age that occurred as a result of the changing operational status of the storage tank. Although the specific results in this study are not directly applicable to other distribution networks, the methods used herein provide guidance on improving the calibration of a network that contains degraded pipe. The results from this study illustrate that it is important to be

mindful of the discrepancies that can arise if changes in the flow area of an aged pipe are ignored when modeling water age. Applying these results in the right manner can improve the modeling of water quality by improving the accuracy of modeled water ages.

CHAPTER IV

APPLICATION OF THREE RANS TURBULENCE MODELS TO AGED WATER TRANSMISSION PIPES[2]

Abstract

The Reynolds-Averaged Navier-Stokes equations were solved to model flow through two aged pipes at Reynolds numbers ranging from 6700 to 31,000. Turbulence models employed include a 4-equation $v^2 - f$ model, and 2-equation realizable $k - \varepsilon$ and $k - \omega$ models. Each of the aged pipes was previously subjected to experimental testing. The $v^2 - f$ turbulence model was found to more accurately reproduce experimental results compared to the realizable $k - \varepsilon$ and $k - \omega$ turbulence models. Overall, the $v^2 - f$ model produced Darcy-Weisbach friction factors ranging from 5% higher to 15% lower than the values obtained from experimental testing. Much of the error is likely attributable to deficiencies in modeling complex flow structures with flow separation and wall roughness elements smaller than the grid scale.

Introduction

Irregular three-dimensional boundaries exist in a variety of engineering applications. Frequently, hydraulic surfaces that were originally manufactured smooth can develop irregular surfaces over time as a result of corrosion, deposition, and accretion. These degradation processes commonly occur in pipes used to transport

[2] Coauthored by Ryan T. Christensen, Robert E. Spall, Ph.D., and Steven L. Barfuss, P.E.

fluids, where the dominant process is a function of pipe material, fluid properties, and the presence of suspended material in the fluid flow. One common situation in which conditions can be favorable for the formation of irregular buildup on a surface occurs when water is transported in ferrous pipes. Ferrous pipes corrode when they come in contact with water and, in extreme cases, corrosion can lead to the formation of a pipe wall surface characterized by increased roughness and irregular form. The resulting irregular boundary greatly complicates the flow dynamics of water moving through a pipe. The ability to describe complex three-dimensional flows in pipes with irregular boundaries is essential in a number of fields. Examples include: the transport of dissolved materials, the mechanics of suspended particle accretion and subsequent erosion, and fluid mixing. Indeed, numerical modeling has already been used with much success to describe the flow in contact tanks (Wang and Falconer 1998: Khan et al. 2006). Notwithstanding the practical and academic benefits provided by modeling flow through a pipe with irregular boundary surfaces, no research has been conducted on the subject. As a result, this study appears to be the first application of computational fluid dynamics (CFD) modeling to an actual three-dimensional, irregular pipe surface.

While studies addressing three-dimensional, irregular roughness are non-existent, numerous studies have been performed on flows with regularly spaced prismatic roughness elements. Of those studies, the majority have focused on two-dimensional roughness. For example, various researchers have considered the effects of fins (cf. Patankar et al. 1979; Zeitoun and Hegazy 2003; Yucel and Dinler 2006), ribs

(cf. Acharya et al. 1994; Rhodes and Senior 2000; Vijiapurapu and Cui 2006), and wavy walls (cf. Russ and Beer 1997; Mahmud et al. 2003) on fluid flow in pipes and channels. Additionally, prismatic three-dimensional roughness has been studied in the form of dimpled surfaces (cf. Mahmood et al. 2001; Park and Ligrani 2005). The study by Acharya et al. (1994) included notable comparisons between experimental studies, a standard $k-\varepsilon$ model, and a nonlinear $k-\varepsilon$ model for flow in a ribbed pipe. Both $k-\varepsilon$ models were found to perform well in the core flow regions and poorly in the separated regions and shear-layer regions near the ribs. However, the non-linear model did give more realistic predictions for mean velocities in the upper shear layer and improved the modeling of streamwise turbulent intensity. The nonlinear model also exhibited better accuracy in the calculation of turbulent kinetic energy production and dissipation in the reattachment region.

Each of the previously cited studies was conducted on a surface with relatively large roughness elements that, due to their size, could be resolved by the surface mesh. However, real pipe surfaces generally have a range of roughness scales with the smallest roughness elements much too small to resolve. Meshing such a surface effectively filters out the smallest roughness elements. Researchers have attempted to account for the effects of small scale roughness elements in a variety of ways. Multiple researchers (cf. Rotta 1962; Krogstad 1991) have suggested modifications to the calculation of mixing length in order to address flow over rough surfaces. In particular, Krogstad (1991) combined van Driest damping functions (van Driest 1956) with the mixing length

formulation of Michel et al. (1968). Nonetheless, Patel (1998) has noted the application of these formulations to complex flows with separation and to three-dimensional flows is not easily attainable. Another approach to modeling flow over rough surfaces is to explicitly develop model formulations in order to account for surface roughness. The $k-\omega$ model of Wilcox (1998) is an example of this approach and incorporates roughness height dependence into the wall boundary conditions. However, this approach requires prior knowledge of the roughness characteristics of the surface to be modeled.

The irregular three-dimensional boundaries used in this study were obtained from two aged pipes with nominal diameters of 0.025-m and 0.050-m, respectively. Figure 11 is a photograph of the interior pipe wall of the 0.050-m pipe sample. The aged pipes were originally used to transport culinary water and the three-dimensional surfaces in these pipes are a result of an estimated 30 years of use for the 0.025-m pipe and 30-50 years use for the 0.050-m pipe. The 0.025-m and 0.050-m pipes had L/D values of 98 and 56, respectively, where L represents pipe length and D represents nominal pipe diameter. The term "diameter" is actually somewhat misleading when applied to the aged pipes considered for this study given that the pipes no longer had circular cross-sections. The usage of the term "diameter" is maintained purely out of convention.

The analysis of the aged pipes was carried out in the three steps. First, the pipes were subjected to hydraulic testing in a laboratory setting. The hydraulic testing was

Figure 11: Photograph of the longitudinally cut 0.050-m aged pipe

used to determine the relationship between the Darcy-Weisbach friction factor and Reynolds number for each pipe as described in Christensen and Barfuss (2009). After the hydraulic testing, the interior walls of segments of the aged pipes were digitized via three-dimensional laser scanning. Because of numerical limitations the entire pipe lengths tested in the laboratory were not digitized. Instead, only portions of the laboratory tested pipes were digitized such that L/D values for the scanned sections of the 0.025-m and 0.050-m pipes were 26 and 27, respectively. The final stage of the current study was comprised of using the digitized pipe surfaces to provide the wall boundary conditions in performing CFD modeling. The modeling was conducted in order to assess the capabilities of CFD techniques at reproducing the laboratory

measured headloss data for pipes with irregular three-dimensional boundaries. The following sections outline the pipe geometry, computational mesh, and boundary conditions employed in modeling the aged pipes, summarize the numerical method which was utilized, and present the results obtained from the CFD modeling.

Pipe Geometry, Computational Mesh, and Boundary Conditions

Pipe geometry. Because of the complexity of the pipe boundaries, mesh development was a lengthy task that included a generous amount of trial and error. Again, Figure 11 is a photograph of the surface of the 0.050-m pipe that was modeled for this study and provides a general idea of the complex geometry of the tested pipes. The irregular surface of the aged pipe is a result of the buildup of corrosion byproducts on the surface of the pipe and is commonly referred to as tuberculation. The tuberculation dominates the surface profiles of both aged pipes considered in this study. The maximum height of individual tubercles in the aged pipes was about 0.01-m. However, as noted previously for real surfaces, the roughness elements of the aged pipe in Figure 11 have a wide range of sizes. The following paragraphs outline the process of meshing the pipes and specifying the boundary conditions.

Computational mesh. Each of the digitized pipes was divided into upstream and downstream sections. The divisions were made so that the upstream sections were fairly short, with $L/D = 6$ for the 0.025-m pipe and $L/D = 5$ for the 0.050-m pipe. The upstream sections were used to develop the inlet boundary conditions for the

downstream sections, which were used for the primary flow modeling. Consequently, the primary flow modeling of 0.025-m pipe was performed with $L/D = 20$, whereas the 0.050-m pipe was modeled with $L/D = 22$. The following discussion on mesh development corresponds to the meshes used for primary flow modeling, although the shorter sections were meshed in similar manner.

The complexity of the pipe surface necessitated using triangular elements in meshing the wall boundaries. Figure 12 is a cutaway view of the wall boundary mesh of the 0.050-m pipe which corresponds to the section shown in Figure 11. Figure 13 is a rendering of the pipe surface based on the mesh shown in Figure 12. A comparison of Figures 11 through 13 illustrates that the boundary mesh matches the general form of

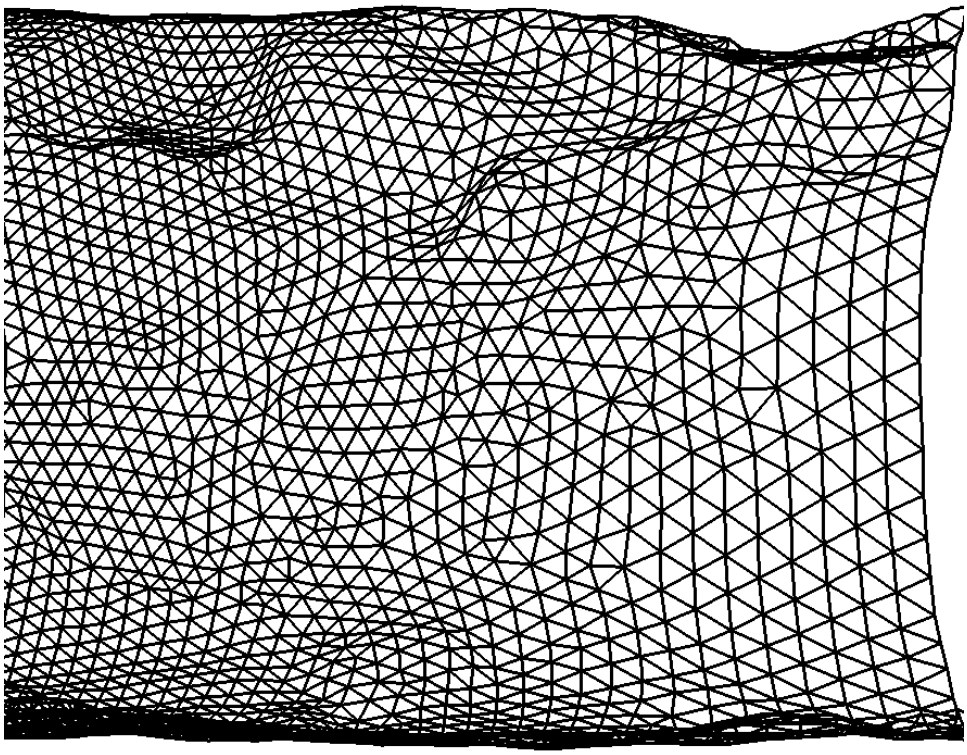

Figure 12: Cutaway view of the wall boundary mesh of the 0.050-m aged pipe

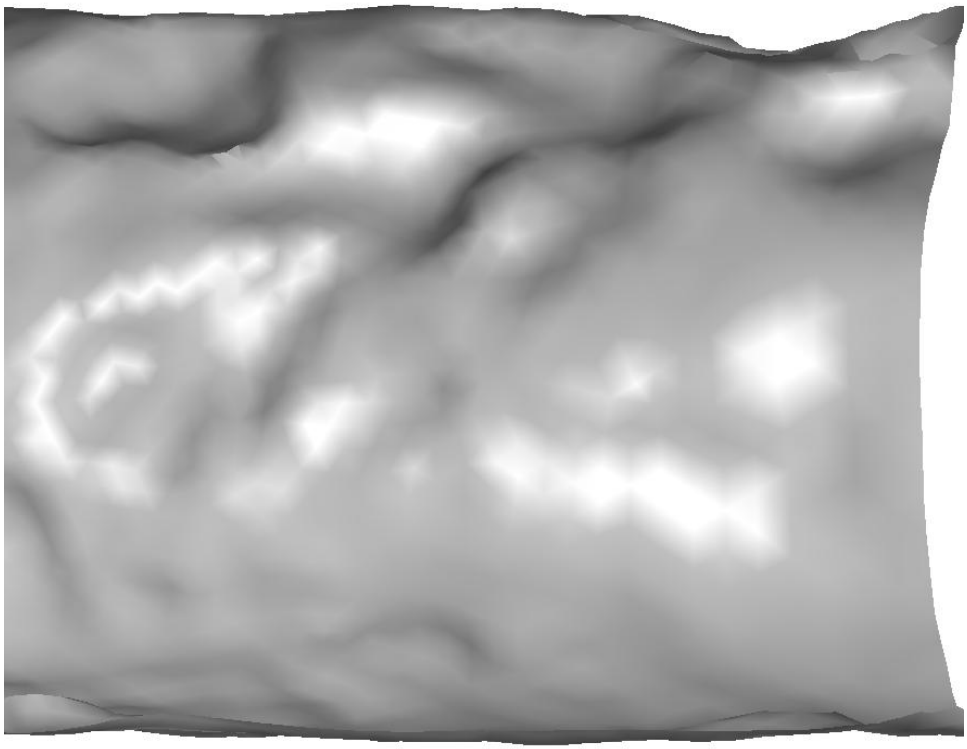

Figure 13: Rendered surface of the 0.050-m aged pipe

the pipe surface very well and highlights the limitations of the surface mesh at capturing the finest details of boundary variation. The surface mesh plainly loses the ability to describe variations in the pipe boundary that are smaller than several times the size of individual mesh elements.

The meshing process was concluded by creating a volume mesh for each pipe. The volume mesh consisted of triangular prisms next to the wall boundary with tetrahedral elements making up the remainder of the interior volume. The triangular prisms facilitated resolution of the near wall region. For the 0.025-m pipe, the height of the first layer was 1.28×10^{-5}-m. A total of fourteen progressively thicker layers completed the near-wall mesh. The prism layers used in meshing the 0.050-m pipe had

a first height of 2.54×10^{-5}-m with a total of ten progressively thicker layers. These values were chosen in order to ensure that average dimensionless wall distance y^+ would be less than one for all of the modeled flow conditions. The dimensionless wall distance is defined as $y^+ = (y \cdot u_\tau)/\nu$ where y is the distance to the nearest wall, ν is the kinematic viscosity, and u_τ is the shear velocity. The shear velocity is defined as $u_\tau = \sqrt{\tau_w/\rho}$ where τ_w is the wall shear stress and ρ is the fluid density. Figure 14 shows a cross-section of the volume mesh used to model flow in the 0.050-m pipe, and

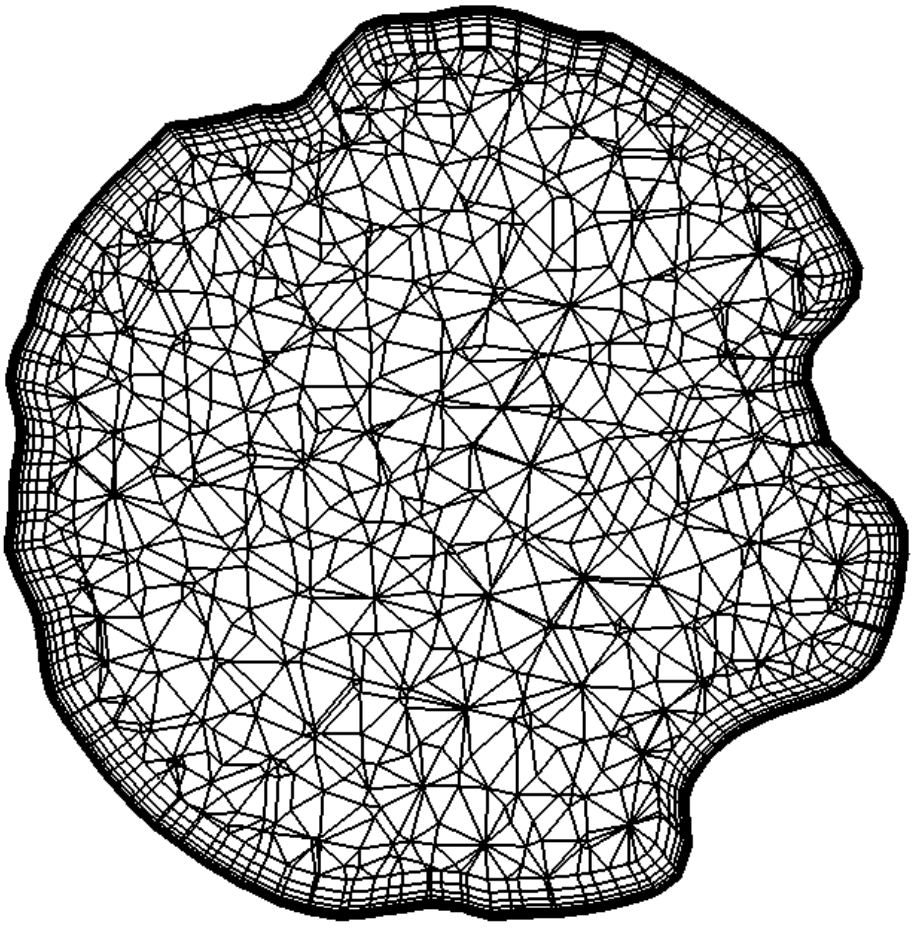

Figure 14: Cross-section showing the mesh of the 0.050-m nominal diameter pipe

illustrates the irregular nature of the aged pipe cross-section as well as the size gradation of the wall bounding prismatic elements. The volume meshes of the 0.025-m and 0.050-m diameter pipes consisted of 2.91×10^6 and 3.06×10^6 cells, respectively. Because the same steps were used in the development of each computational mesh, the meshes for the 0.025-m pipe and the 0.050-m pipe were similar in form.

Boundary conditions. Lacking experimentally measured inlet profiles, special care was taken in developing boundary conditions. Using streamwise periodic boundary conditions, the shorter upstream pipe sections were modeled for each combination of flow rate and turbulence model considered for this study. The outlet flow profiles from the initial pipe section, including x, y, and z velocity components, along with the necessary turbulence parameters, were then exported and used to provide quasi-fully developed inlet flow profiles for the longer, downstream section of pipe (primary modeling section).

Numerical Method

The steady, Reynolds-Averaged Navier-Stokes (RANS) equations were solved using version 6.3.26 of the general purpose CFD code FLUENT (Fluent 2006). A second-order upwind method was used for interpolation of variables to cell faces for the convective terms, whereas diffusive terms were discretized using second-order central differencing. Pressure-velocity coupling was achieved using the SIMPLEC method. Iterative convergence was achieved when the normalized residuals of all discretized transport equations were decreased by 5 orders of magnitude.

The following turbulence models, all based on the Boussinesq approximation to relate the Reynolds stresses to the mean flow, were assessed: a two-equation realizable $k-\varepsilon$ model (Shih et al. 1995), a standard $k-\omega$ model (Wilcox 1998), and a four-equation $k-\varepsilon-v^2-f$ model (Lien and Durbin 1996) (herein referred to as v^2-f). In all cases the models were integrated directly to the wall; that is, no wall functions were used. For the realizable $k-\varepsilon$ model, a two-layer approach was employed. In particular, the one-equation model of (Wolfshtein 1969) was employed in the near-wall, viscosity dominated region defined by $\mathrm{Re_y} < 200$ where $\mathrm{Re_y} = y\sqrt{k}/\nu$ is a turbulent Reynolds number. Outside this region, the realizable $k-\varepsilon$ model was employed. The $k-\omega$ and v^2-f models may be integrated directly to the wall without modification. The 1998 formulation of the Wilcox $k-\omega$ model is in common use, and its equations and standard closure coefficients are well known, hence for purposes of brevity they are not shown. However, the v^2-f and two-layer, realizable $k-\varepsilon$ formulations are less commonly used, and for completeness we present next the transport equations for these two models as implemented in FLUENT (Fluent 2006).

The transport equations for k and ε in the two-layer realizable $k-\varepsilon$ model are given as:

$$\frac{\partial}{\partial x_i}(\rho u_i k) = \frac{\partial}{\partial x_i}\left[\left(\mu + \frac{\mu_t}{\sigma_k}\right)\frac{\partial k}{\partial x_i}\right] + \mu_t S^2 - \rho\varepsilon \tag{8}$$

$$\frac{\partial}{\partial x_i}(\rho u_i \varepsilon) = \frac{\partial}{\partial x_i}\left[\left(\mu + \frac{\mu_t}{\sigma_\varepsilon}\right)\frac{\partial \varepsilon}{\partial x_i}\right] + \mu_t C_1 S\varepsilon - \rho C_2 \frac{\varepsilon^2}{k+\sqrt{\nu\varepsilon}} \tag{9}$$

where ν is the kinematic viscosity, $S = \sqrt{2S_{ij}S_{ij}}$, $S_{ij} = \frac{1}{2}\left(\frac{\partial u_i}{\partial x_j} + \frac{\partial u_j}{\partial x_i}\right)$, $C_1 = max[0.43, \eta/(\eta + 5)]$, and $\eta = Sk/\varepsilon$. The closure coefficients are given as $C_2 = 1.9$, $\sigma_k = 1.0$, and $\sigma_\varepsilon = 1.2$. In the case of the realizable $k - \varepsilon$ model, the turbulent viscosity is given as $\mu_t = \rho C_\mu k^2/\varepsilon$ where the value of C_μ is not constant but given (for a non-rotating reference frame) by $C_\mu = 1/\left(A_0 + A_s \frac{kU^*}{\varepsilon}\right)$ where $U^* = \sqrt{S_{ij}S_{ij} + \Omega_{ij}\Omega_{ij}}$ and $\Omega_{ij} = \frac{1}{2}\left(\frac{\partial u_i}{\partial x_j} - \frac{\partial u_j}{\partial x_i}\right)$ is the mean rate-of-rotation tensor. In addition, $A_0 = 4.04$ and $A_s = \sqrt{6}\cos\phi$ where $\phi = \frac{1}{3}\cos^{-1}\left(\sqrt{6}W\right)$, and $W = S_{ij}S_{jk}S_{ki}/\left(S_{ij}S_{ij}\right)^{3/2}$. The transport equations for both k and ε are solved in the fully turbulent region ($\mathrm{Re_y} > 200$). In the near-wall region ($\mathrm{Re_y} < 200$) the transport equations for momentum and turbulence kinetic energy are solved, however the turbulent viscosity is computed algebraically as $\mu_t = \rho C_\mu l_\mu \sqrt{k}$. Here, the length scale is computed as $l_\mu = yC_l^*\left(1 - e^{-\mathrm{Re_y}/A_\mu}\right)$. This near-wall turbulent viscosity is blended with the turbulent viscosity computed in the fully turbulent region. In addition, the value of ε in the near wall region is computed algebraically as $\varepsilon = k^{3/2}/l_\varepsilon$ where the length scale is computed as $l_\varepsilon = yC_l^*\left(1 - e^{-\mathrm{Re_y}/A_\varepsilon}\right)$. The values of ε computed using the algebraic formulation and the transport equation are blended to ensure a smooth transition near $\mathrm{Re_y} = 200$. The closure coefficients for the near wall model are $C_l^* = \kappa C_\mu^{-3/4}$, $\kappa = 0.41$, $C_\mu = 0.09$, $A_\mu = 70$, and $A_\varepsilon = 2C_l^*$.

The transport equation for k in the $v^2 - f$ model is identical to equation (8).

The equation for ε is given as:

$$\frac{\partial}{\partial x_i}(\rho u_i \varepsilon) = \frac{C_{\varepsilon 1}^* \mu_t S^2 - C_{\varepsilon 2}\rho\varepsilon}{T} + \frac{\partial}{\partial x_i}\left[\left(\mu + \frac{\mu_t}{\sigma_\varepsilon}\right)\frac{\partial \varepsilon}{\partial x_i}\right] \quad (10)$$

The turbulent viscosity is given by the relationship $\mu_t = \rho C_\mu \overline{v^2} T$ where T is a turbulent time scale given as:

$$T = min\left[T^*, \frac{\chi}{\sqrt{3}}\frac{k}{\overline{v^2} C_\mu \sqrt{2 S_{ij} S_{ij}}}\right] \quad (11)$$

where,

$$T^* = max\left[\frac{k}{\varepsilon}, 6\sqrt{\frac{\nu}{\varepsilon}}\right] \quad (12)$$

The governing equations for $\overline{v^2}$ and f are written as:

$$\frac{\partial}{\partial x_i}\left(\rho u_i \overline{v^2}\right) = \rho k f - 6\rho\overline{v^2}\frac{\varepsilon}{k} + \frac{\partial}{\partial x_i}\left[\left(\mu + \frac{\mu_t}{\sigma_k}\right)\frac{\partial \overline{v^2}}{\partial x_i}\right] \quad (13)$$

$$f - L^2\frac{\partial^2 f}{\partial x_i^2} = (C_1 - 1)\frac{2/3 - \overline{v^2}/k}{T} + C_2\frac{\mu_t S^2}{\rho k} + \frac{5\overline{v^2}/k}{T} \quad (14)$$

where the length scale, L, appearing in the elliptic relaxation equation for f is given as:

$$L = C_L\, max\left[L^*, C_\eta\left(\frac{\nu^3}{\varepsilon}\right)^{1/4}\right] \quad (15)$$

$$L^* = min\left[\frac{k^{3/2}}{\varepsilon}, \frac{1}{\sqrt{3}}\frac{k^{3/2}}{\overline{v^2}C_u\sqrt{2S_{ij}S_{ij}}}\right] \quad (16)$$

The closure coefficients are $\chi = 0.6$, $C_1 = 1.4$, $C_2 = 0.3$, $C_{\varepsilon 1} = 1.4$, $C_{\varepsilon 2} = 1.9$, $C_\eta = 70$, $C_\mu = 0.22$, $C_L = 0.23$, $\sigma_k = 1.0$, $\sigma_\varepsilon = 1.3$, and $C_{\varepsilon 1}^* = C_{\varepsilon 1}\left(1 + 0.045\sqrt{k/\overline{v^2}}\right)$. Note that the wall boundary conditions for equations 6 and 7 are given as $\overline{v^2} = 0$ and $f = 0$.

Results

Explanation and validation. The 0.025-m pipe was modeled at $\mathrm{Re} = 13{,}000$ while the 0.050-m pipe was modeled at both $\mathrm{Re} = 6700$ and $\mathrm{Re} = 31{,}000$. Bulk Reynolds numbers were calculated as $\mathrm{Re} = U_{bulk} \cdot L_c/\nu$ where U_{bulk} represents a bulk velocity and L_c is a characteristic length. The characteristic length used in this work was $L_c = \sqrt{(4 \cdot \forall/L) \cdot \pi}$ where $\forall$ represents the volume of the solution domain and L represents the length of the pipe section. This expression for the characteristic length was obtained by manipulating the equation for the volume of a cylinder ($\forall = \pi \cdot D^2/4 \cdot L$) with the characteristic length L_c substituted for the pipe diameter D. Thus, the characteristic length represents the diameter of a smooth cylinder that will have the same length and volume as the pipe test section.

During the solution process, mesh independence was assessed by first computing the pipe flow using base-level meshes, each having approximately 3×10^6 cells, and then adapting the meshes based on strain rate so that the refined meshes contained approximately 4×10^6 cells. Gradient adaptation was utilized using a curvature

option such that the second gradients of strain rate were used in adapting the meshes. In addition to the strain-based adaptation, the mesh dependence was also assessed by converting the base level mesh to polyhedra. The polyhedral mesh was modeled for a single Reynolds number ($\mathrm{Re} = 31{,}000$) using the $v^2 - f$ model. Table 3 shows the percent change in pressure drop (from pipe inlet to pipe outlet) between the results found using the original and adapted meshes. For most cases the percent change in pressure drop was about 1% or less. The largest percentage change was found for flow modeled using the $v^2 - f$ model in the 0.050-m pipe with $\mathrm{Re} = 6700$ (3.88%). Ultimately, because there was little change between the results obtained using the base-level and adapted meshes, the base-level mesh results were chosen for presentation.

When integrating turbulence models to the wall, the y^+ values for the wall adjacent cells should be approximately one or less in order to adequately resolve the viscous sublayer. Average wall y^+ was determined by calculating the area weighted average of y^+ over the wall boundary. In addition, maximum values of y^+ were reviewed for each flow condition. Table 4 summarizes the average and maximum values for y^+ for each combination of flow rate and turbulence model. Average y^+ was

Table 3: Percent Change in Pressure Drop

@	$\mathrm{Re} = 13{,}000$	$\mathrm{R} = 6700$	$\mathrm{Re} = 31{,}000$
realizable $k - \varepsilon$	1.01	0.119	1.21
$k - \omega$	0.518	1.44	1.40
$v^2 - f$	0.630	3.88	0.540
$v^2 - f$ w/polyhedra	N/A	N/A	2.33

Table 4: Average and Maximum Values of y^+ for Each Flow Condition

Pipe	Re	avg. y^+	max. y^+
0.025-m	13,000	0.23	0.37
0.050-m	6700	0.12	0.35
0.050-m	31,000	0.42	1.19

found to be less than one for all modeled flow condition. The maximum calculated value of y^+ was 1.19, corresponding to the 0.050-m pipe with $\mathrm{Re} = 31{,}000$.

The momentum integral equation was used to provide insight into the results of the three turbulence models differed. The steady Reynolds averaged Navier-Stokes equation for x-direction momentum can be written, including the Boussinesq approximation for turbulent stresses, as:

$$\frac{\partial}{\partial x}\rho uu + \frac{\partial}{\partial y}\rho uv + \frac{\partial}{\partial z}\rho uw = -\frac{\partial}{\partial x}\left(p + \frac{2}{3}\rho k\right) + \frac{\partial}{\partial x}\left(2\mu_t \frac{\partial u}{\partial x}\right) + \frac{\partial}{\partial y}\left[\mu_t\left(\frac{\partial v}{\partial x} + \frac{\partial u}{\partial y}\right)\right] + \frac{\partial}{\partial z}\left[\mu_t\left(\frac{\partial w}{\partial x} + \frac{\partial u}{\partial z}\right)\right] \quad (17)$$

Integrating the left had side of Equation 17 over the computational domain (control volume) and applying the divergence theorem results in an expression for momentum flux across the control volume surfaces. Moreover, integration of the right had side of Equation 17 provides the forces that act on the solution control volume. The resulting expression is given as:

$$\int_{cs} u\left(\rho\vec{V}\cdot\vec{n}\right) dA = \sum F_x \quad (18)$$

For the modeled pipes, the external forces are due to modified pressure and normal viscous stresses at the inlet and outlet, and pressure and viscous drag along the pipe wall. Table 5 is a tabulation of the components in Equation 17. The forces resulting from the normal viscous stresses have been omitted from Table 5 because they are several orders of magnitude less than the other contributing forces. In addition to the rough pipes, smooth pipe solutions obtained using the realizable $k - \varepsilon$ turbulence model have been included in Table 5 for comparison. A review of the momentum flux and force data reveals several significant generalizations. First, the large disparity in magnitude between the pressure drag forces and the viscous drag forces clearly indicates that pressure drag is the dominant resistive mechanism within the aged pipe sections. Furthermore, the pressure drag was fairly uniform while the viscous drag varied widely. Specifically, there were no cases where the percent deviation from mean of the pressure drag was greater than 0.3%, whereas the percent deviation from mean for viscous drag forces often exceeded 30%. While pressure drag was important in the rough aged pipes, the smooth pipes are subjected to only viscous drag. Moreover, of the three turbulence models utilized in calculating flow in the rough pipes, the magnitudes of the viscous forces calculated by the $k - \omega$ turbulence model were most similar to the magnitudes of the viscous forces in the smooth pipes. Lastly, it is observed that the $v^2 - f$ model produced the largest drag values for nearly every category in Table 5 with this trend particularly pronounced for the viscous drag forces.

Table 5: Summary of Forces and Momentum Flux

	Momentum (kg-m/s^2)		Net Pressure force (In – Out) (N)	Pressure Drag Force (N)	Viscous Drag Force (N)
0.025-m pipe @Re=13,000	**in**	**out**			
realizable $k-\varepsilon$	2.428E-1	2.584E-1	11.3272	11.2258	8.63E-2
$k-\omega$	2.441E-1	2.654E-1	11.3293	11.2320	7.66E-2
v^2-f	2.275E-1	2.651E-1	11.4068	11.2487	1.224E-1
smooth	9.64E-2	9.64E-2	6.67E-2	0	6.67E-2
0.050-m pipe @Re=6700					
realizable $k-\varepsilon$	9.42E-02	1.01E-01	38.3802	38.3296	4.39E-2
$k-\omega$	1.01E-01	1.05E-01	38.3435	38.3098	3.05E-2
v^2-f	9.87E-02	1.03E-01	38.3922	38.3262	6.18E-2
smooth	8.86E-02	8.86E-02	3.18E-2	0	3.18E-2
0.050-m pipe @Re=31,000					
realizable $k-\varepsilon$	2.0027	2.1250	40.0627	39.4649	4.772E-1
$k-\omega$	2.0862	2.1841	39.8529	39.3833	3.797E-1
v^2-f	2.0211	2.1900	40.4575	39.5600	7.355E-1
smooth	1.8712	1.8712	4.206E-01	0	4.205E-1

Laboratory data comparisons. Comparison between the CFD models and the laboratory testing was performed in terms of the Darcy-Weisbach friction factor. Presented in Table 6 are the Darcy-Weisbach friction factors determined from laboratory testing and CFD modeling. The friction factors calculated from the experimental results of the 0.050-m pipe at $\mathrm{Re} = 6700$ and $\mathrm{Re} = 31{,}000$ exhibit near Reynolds number independence, indicating fully rough flow. In general, the friction

Table 6: Comparison of Darcy-Weisbach Friction Factors

Method	0.025-m pipe @Re=13,000	0.050-m pipe @Re=6700	0.050-m pipe @Re=31,000
experimental	1.57E-01	1.13E-01	1.08E-01
realizable $k-\varepsilon$	1.13E-01	1.04E-01	7.67E-02
$k-\omega$	1.13E-01	6.97E-02	6.76E-02
v^2-f	1.35E-01	1.18E-01	9.22E-02

factors calculated for the 0.025-m pipe were somewhat higher than the friction factors calculated for the 0.050-m pipe indicating that the 0.025-m pipe had a larger relative roughness than the 0.050-m pipe.

The friction factors calculated using the $v^2 - f$ model showed significantly better agreement with the experimental results than the friction factors from the realizable $k - \varepsilon$ and standard $k - \omega$ models. The friction factors computed using the $v^2 - f$ model ranged from 5% higher to 15% lower than those obtained from laboratory data. Moreover, the realizable $k - \varepsilon$ and standard $k - \omega$ models exhibited similar performance for each of the two higher Reynolds number flows, but the realizable $k - \varepsilon$ model was superior for the 0.050-m pipe with $\mathrm{Re} = 6700$. While the $k - \omega$ model was generally inferior to the other models at matching the experimental results, it was the most successful of the three turbulence models at reproducing the Reynolds number independence of the experimental results for the 0.050-m pipe. In contrast, the friction factors calculated using the realizable $k - \varepsilon$ and $v^2 - f$ model results both showed greater Reynolds number dependence.

Perhaps the most important observation is that, with a single exception, the turbulence models always under-predicted the Darcy-Weisbach friction factor (and by extension the headloss). Two possible causes for this chronic under prediction of the Darcy-Weisbach friction factor are deficiencies in modeling complex flows and the inability to fully resolve the smallest elements of the rough boundary surface. As noted previously, the $v^2 - f$ model consistently calculated higher drag forces than the other

turbulence models. This, combined with the fact that nearly all friction factors were under-predicted, resulted in the $v^2 - f$ model providing the most accurate friction factors and suggests that the $v^2 - f$ model may be more capable at computing complex flows with separation and three-dimensional flow structures.

Plots of $v^2 - f$ model results. Plots showing contours of normalized velocity magnitude and normalized turbulence kinetic energy are shown for each flow condition computed using the $v^2 - f$ model. Shown in Figure 15 are contours of normalized velocity for the 0.025-m pipe at $\mathrm{Re} = 13{,}000$. The effects of the irregular boundary on the velocity profile are apparent as it is highly distorted. Contours of normalized turbulence kinetic energy, shown in Figure 16, are also highly distorted as a result of the

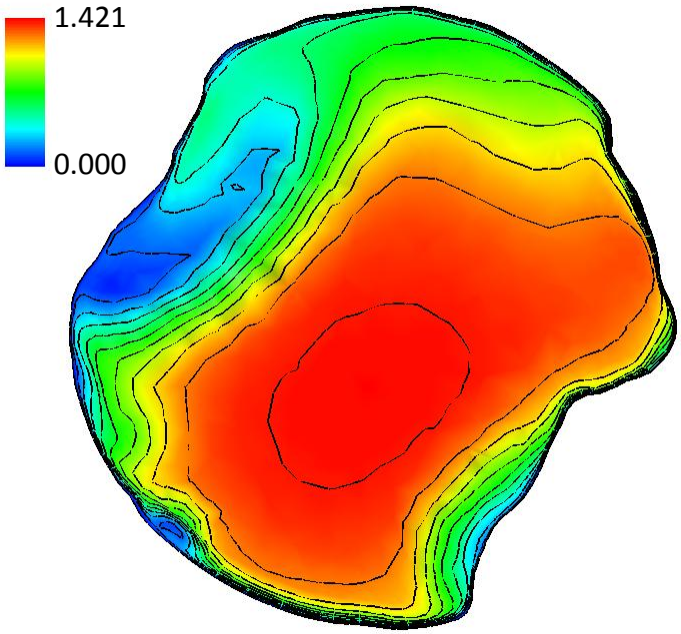

Figure 15: Velocity distribution normalized by bulk velocity for the 0.025-m pipe at $\mathrm{Re} = 13{,}000$. Contours – min = 0, max = 1.40, interval = 0.14

wall boundary with local maxima seen at irregular intervals around the edges of the pipe wall. Shown in Figures 17 and 18 are plots of normalized velocity contours for flow in the 0.050-m pipe with $\mathrm{Re} = 6700$ and $\mathrm{Re} = 31{,}000$, respectively. The two plots are very similar; however, subtle differences can be seen in the velocity gradient perpendicular to the streamwise direction. In the core region of flow the velocity gradient is higher for the case with $\mathrm{Re} = 6700$ than for $\mathrm{Re} = 31{,}000$. Near the wall, the conditions are reversed with the velocity gradient higher for $\mathrm{Re} = 31{,}000$. Likewise, Figures 19 and 20 show similar results with respect to turbulence kinetic energy. The gradient of turbulence kinetic energy perpendicular to the streamwise direction in the

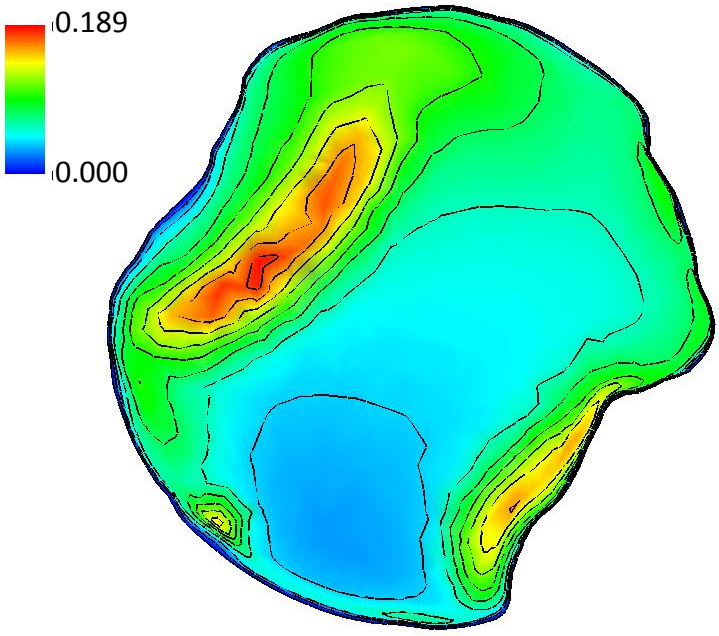

Figure 16: Turbulence kinetic energy distribution normalized by $U_{bulk}^2/2$ for the 0.025-m pipe at $\mathrm{Re} = 13{,}000$. Contours – min = 0, max = 0.18, interval = 0.02

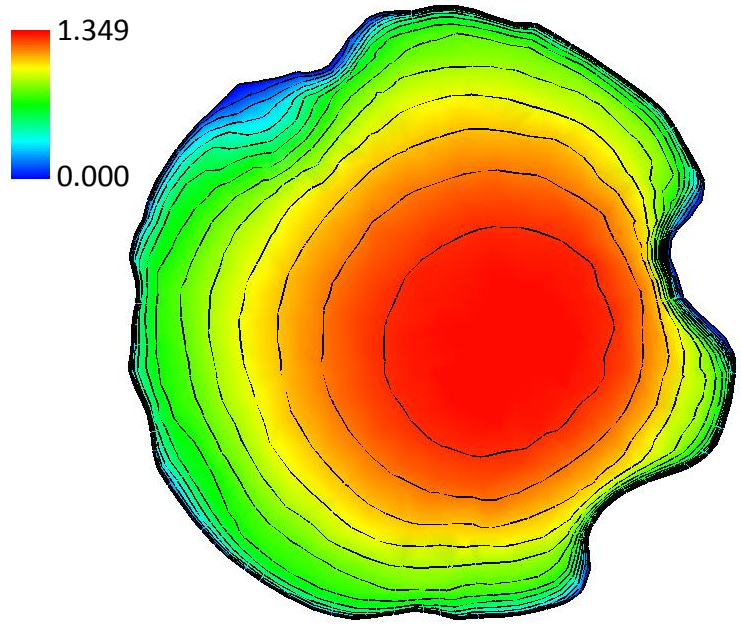

Figure 17: Velocity distribution normalized by bulk velocity for the 0.050-m pipe at $\mathrm{Re} = 6700$. Contours – min = 0, max = 1.30, interval = 0.10

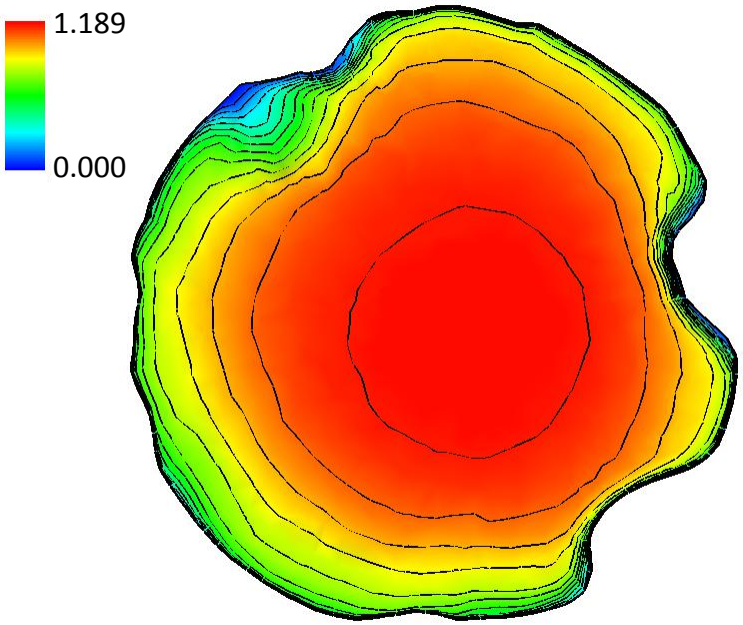

Figure 18: Velocity distribution normalized by bulk velocity for the 0.050-m pipe at $\mathrm{Re} = 31{,}000$. Contours – min = 0, max = 1.17, interval = 0.09

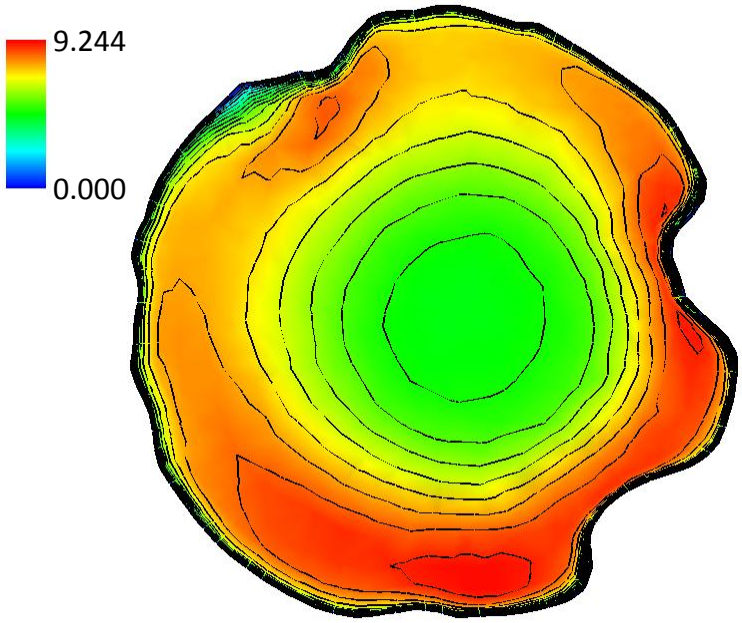

Figure 19 Turbulence kinetic energy distribution normalized by $U_{bulk}^2/2$ for the 0.050-m pipe at $\mathrm{Re} = 6700$. Contours – min = 0, max = 9.0, interval = 0.60

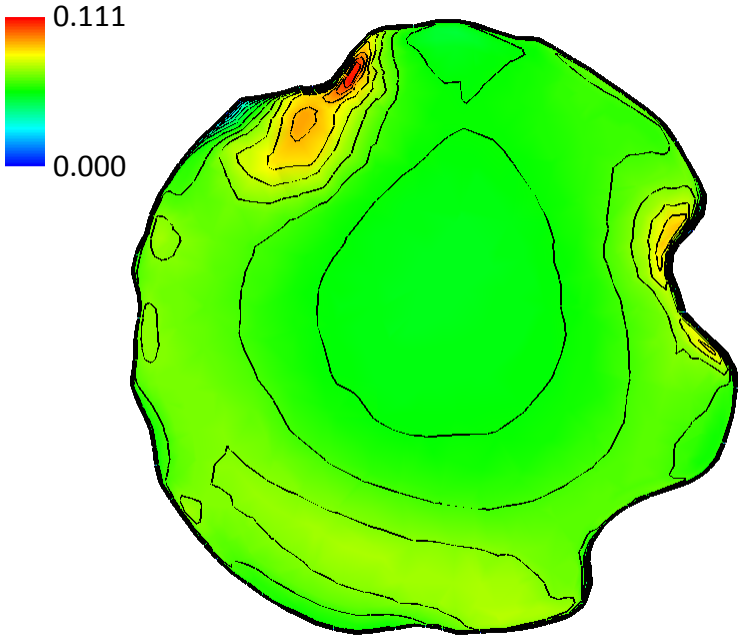

Figure 20: Turbulence kinetic energy distribution normalized by $U_{bulk}^2/2$ for the 0.050-m pipe at $\mathrm{Re} = 31{,}000$. Contours – min = 0, max = 0.105, interval = 0.007

core region of flow is higher for $\mathrm{Re} = 6700$, whereas in the near wall region the gradient is higher for $\mathrm{Re} = 31{,}000$.

Conclusions

Pipes with irregular, rough boundaries are common in a variety of engineering applications. In spite of their ubiquity very few numerical studies have dealt with pipes that have three-dimensional irregular roughness. Obtaining accurate surface representations, meshing the computational domain, and model convergence are all complicated by irregular boundary surfaces. Nevertheless, CFD modeling offers many potential benefits in understanding the phenomena that occur in aged pipes with the eventual application of that understanding to pipe network models where pipe degradation is a problem.

The $v^2 - f$ model was the best performer of the three models considered in this study. Specifically, the $v^2 - f$ model was most accurate for the 0.050-m pipe with $\mathrm{Re} = 6700$. At higher Reynolds numbers the $v^2 - f$ model under-predicted the Darcy-Weisbach friction factor by about 15%. With a single exception, all of the CFD models under-predicted the Darcy-Weisbach friction factor. Pressure drag was found to be the dominant resistive force in the pipes. For this reason deficiencies in calculating flow separation are a likely culprit for the near-universal under prediction of the friction factor along with shortcomings in resolving the smallest roughness elements.

Despite current limitations, CFD modeling has been shown to be a powerful tool in better understanding flow in aged, rough pipes. While not perfect, these tests

indicate that CFD modeling can be used successfully to model flow in spite of the irregular boundaries in aged pipes. The velocity and turbulence kinetic energy profiles presented in this work would be very difficult to obtain without CFD, yet have the potential to benefit many disciplines where aged pipe are in use. Specific advancements that could improve modeling accuracy include better predictions of flow separation at high Reynolds numbers and improved methods to account for the smallest roughness elements that cannot be resolved by the boundary mesh.

CHAPTER V

APPLICATION OF LARGE EDDY SIMULATION TO AGED WATER TRANSMISSION PIPES[3]

Abstract

The filtered Navier-Stokes equations were solved using the techniques of large eddy simulation to model flow through an aged pipe at a Reynolds number of 6800. The large eddy simulation produced Darcy-Weisbach friction factors that were 20% less than the friction factors obtained from experimental tests. Much of the error is believed to be a consequence of filtering the smallest roughness elements when meshing the pipe wall boundary and possible deficiencies in the subgrid-scale model at modeling the complex flow three-dimensional flow structures due to the irregular pipe boundary.

Introduction

Three-dimensional irregular surfaces are present in a variety of engineering applications. In addition, many surfaces that are originally manufactured smooth become rough over time as a result of corrosion, deposition, accretion and other degradation processes. When ferrous pipes are used to transport water, conditions are often favorable for the formation of rough, irregular surfaces. As a result of aging, the changes in the interior surface profile of water transporting pipes can be extreme, with the development of an irregular boundary greatly influencing the flow dynamics of

[3] Coauthored by Ryan T. Christensen, Robert E. Spall, Ph.D., and Steven L. Barfuss, P.E.

water transported by degraded pipes. Understanding the complex flow dynamics resulting from irregular surfaces is crucial to the explanation of many flow processes that occur in aged pipes. Dissolved material transport, sediment transport, and fluid mixing are a few of the processes that would benefit from a more detailed characterization of flow.

Computational fluid dynamics (CFD) uses numerical methods to compute flow by solving the Navier-Stokes equations. For many flow processes, the turbulent fluctuations of real fluid flow play an important role in the modeling of the process. Two primary CFD techniques exist for resolving the turbulent fluctuations of fluid flow: direct numerical simulation (DNS) and large eddy simulation (LES). DNS requires the resolution of all spatial and temporal scales within a flow. Consequently, despite continuing advancements in computers, DNS is infeasible for describing the highly complex flows that occur along the interior walls of aged pipes (Moin and Mahesh 1998). In LES, the motion of the large eddies is directly calculated while a subgrid-scale model is used to describe the smaller eddies. This reduction in model complexity allows LES to be applied to a much greater range of flows than DNS (Piomelli 1999). While the practical and academic benefits provided by modeling flow through a pipe with irregular boundary surfaces are clear, this appears to be the first application of LES to an actual three-dimensional, irregular surface. Notwithstanding the lack of studies related to irregular surfaces, the utility of LES has been demonstrated as several open channel

flows have been modeled in order to study sediment transport (McCoy et al. 2008; Stoesser et al. 2008; Teruzzi et al. 2009).

Unger and Friedrich (1991) were the first to use the techniques of LES to model turbulent flow in a straight pipe. Their study was conducted on a smooth, straight pipe with a bulk Reynolds number of approximately $\mathrm{Re} = 50{,}000$ using a cylindrical coordinate mesh and found the calculated mean velocity profiles and root mean square velocity components to be in good agreement with experimental data. The next application of LES to turbulent flow in a smooth pipe was performed by Eggels (1994), who also utilized a cylindrical coordinate system. Eggels evaluated the effects of varying LES model parameters over multiple test runs. The parameters varied by Eggels included grid spacing, various model constants, methods for modeling near wall turbulence, etc. (for a full list see Eggels 1994). In general, the results obtained were in good agreement with experimental data. Rudman and Blackburn (1999) performed LES on turbulent flow in a circular pipe but utilized a Cartesian grid with a spectral element spatial discretization in order to assess the application of LES to complex geometries. While Rudman and Blackburn (1999) were successful at reproducing experimental measurements of mean velocity, velocity fluctuations, and shear stress, the numerical scheme employed in their study required prior knowledge of the wall shear stresses. As a result, their methods are not generally applicable to more complex flows.

Various researchers have extended the study of LES in pipes beyond the standard case of a smooth, straight pipe. Vijiapurapu and Cui (2006) conducted a

notable study on pipe flow that applied LES to ribbed pipes with different rib densities. The results of Vijiapurapu and Cui agreed well with rib roughness calculations based on laboratory experiments and, as a result, demonstrated the utility of LES in describing complex flows with separation. Further studies in which LES has been applied to fluid flow in pipes have included curved pipes (Boersma and Nieuwstadt 1996) and rotating pipes (Eggels and Nieuwstadt 1993; Yang and McGuirk 1999; Feiz et al. 2002). All of the previous studies cited herein utilized either the Smagorinksy subgrid-scale model (Smagorinksy 1963) or the dynamic Smagorinsky subgrid-scale model of Germano et al. (1991) and Lilly (1992). Furthermore, each study was conducted using an idealized pipe surface that was either smooth, or in the case of Vijiapurapu and Cui (2006), a surface with roughness elements that were identical and sufficiently large to be resolved by the surface mesh. Real surfaces, on the other hand, often have a range of roughness scales with the smallest roughness elements much too small to be resolved by a reasonably sized boundary mesh. As a result, meshing a real surface filters out the smallest roughness elements. As there are no methods for overcoming this limitation when performing LES, assessing the impact on accuracy of neglecting the small, unresolvable elements was an important topic for this study.

The aged pipe in this study had a nominal diameter of 0.050-m. The pipe was originally used to transport culinary water and the irregular three-dimensional boundary surface of the pipe was a result of degradation occurring over an estimated 30-50 years of use. The pipe section had a dimensionless length of $L/D = 56$, where L represents

pipe length and D represents nominal inside diameter. Though used throughout this study, the term "diameter" is somewhat misleading since the pipe considered for this study had a non-circular cross-section. Nevertheless, the term "diameter" is maintained out of convention and for simplicity.

The pipe was subjected to hydraulic testing in a laboratory setting to first establish its headloss characteristics. In particular, the hydraulic testing was used to determine the relationship between the Darcy-Weisbach friction factor and Reynolds number using the procedure described in Christensen and Barfuss (2009). After hydraulic testing, a segment of the aged pipe was digitized via three-dimensional laser scanning of the interior pipe surface. The surface scanning of the aged pipe provided highly accurate three-dimensional digital representations of the internal pipe boundary which provided the wall boundary conditions for the CFD calculations. While the laboratory testing was conducted on a pipe section with $L/D = 56$, computational resource limitations necessitated a length of $L/D = 6$ for performing the LES. The following sections outline the pipe geometry, mesh, and boundary conditions employed in modeling the aged pipes, describe the numerical method which was utilized, and present the results obtained from the LES.

Pipe Geometry, Mesh, and Boundary Conditions

Pipe geometry. Because of the complexity of the pipe wall boundary, mesh development was a lengthy task that included considerable trial and error. The surface

of the 0.050-m pipe modeled in this study is shown in Figure 21 and illustrates the complex geometry of the tested pipes. The largest roughness elements were observed to have a height of approximately 0.01-m. While the largest roughness elements clearly dominate the surface profile of the aged pipe, Figure 21 also illustrates the wide range in roughness element size. The following paragraphs outline the development of the computational mesh and specify the boundary conditions.

Computational mesh. The complexity of the pipe surface necessitated using triangular elements in meshing the wall boundaries. Figure 22 is a cutaway view of the wall boundary mesh corresponding to the pipe section shown in Figure 21. Figure 23 is a rendering of the pipe surface based on the mesh shown in Figure 21. A comparison of Figures 21 through 23 demonstrates how well the boundary mesh matches the general

Figure 21: Photograph of the surface of the 0.050-m pipe

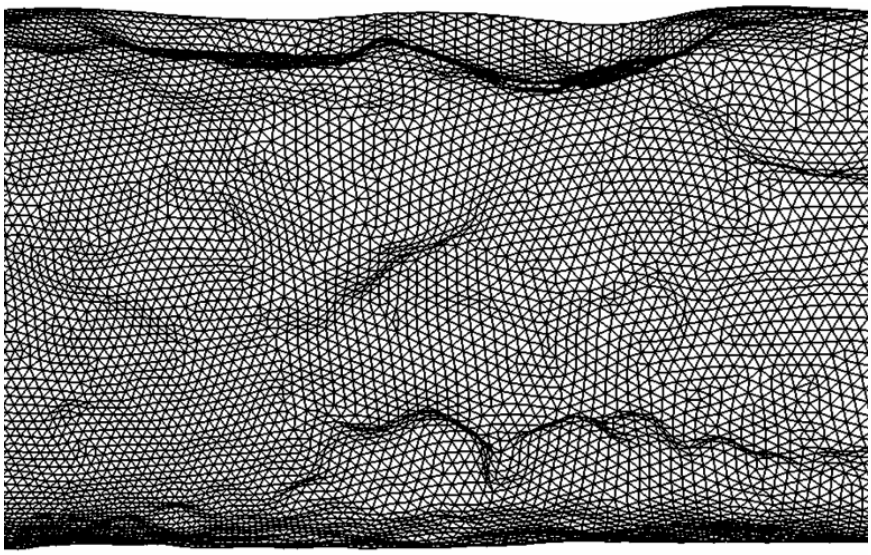

Figure 22: Cutaway view of the wall boundary mesh of the 0.050-m pipe

form of the pipe surface as well as highlights the limitations of the surface mesh at capturing the finest details of boundary variation. While the larger roughness elements are described very well by the surface mesh, the resolution of the smaller roughness elements ranges from partial to nonexistent depending on roughness element size.

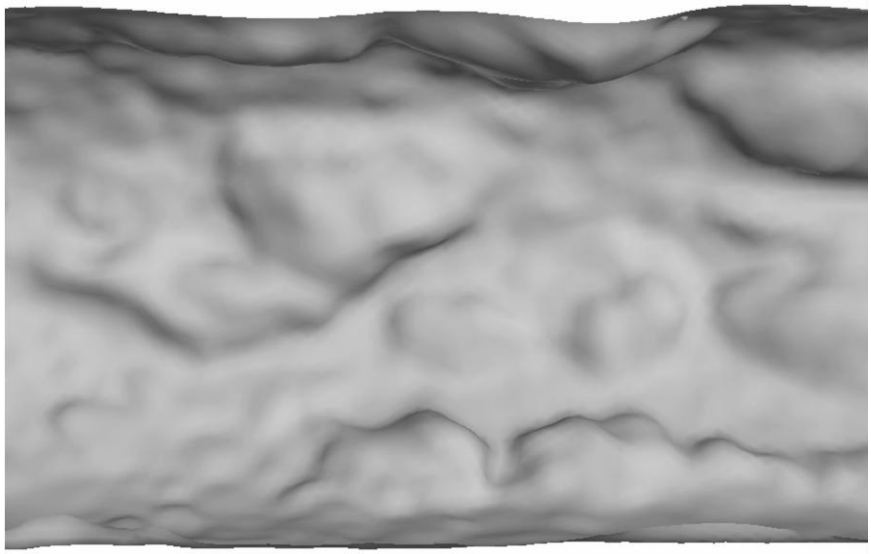

Figure 23: Rendering of the 0.050-m pipe

The meshing process was concluded with the creation of the volume mesh. The volume mesh consisted of 12 layers of progressively thicker triangular prisms next to the wall boundary, followed by two layers of pyramids which enabled the transition to the hexahedral elements making up the bulk of the interior volume. The initial 12 layers of triangular prisms facilitated resolution of the boundary layer. To this end, the height of the first prism layer was 2.54×10^{-5}-m. This value was chosen in order to ensure an average dimensionless wall distance of $\mathrm{y}^+ \leq 1$ during flow simulation. The dimensionless wall distance is defined as $\mathrm{y}^+ = (y \cdot u_\tau)/\nu$ where y is the distance to the nearest wall, ν is the kinematic viscosity, and u_τ is the shear velocity. The shear velocity is defined as $u_\tau = \sqrt{\tau_w/\rho}$ where τ_w is the wall shear stress and ρ is the fluid density. Figure 24 shows a cross-section of the volume mesh used to model flow in the 0.050-m pipe, illustrating the irregular nature of the pipe cross-section and the size gradation of the wall bounding prismatic elements. The finished volume mesh consisted of 1.7×10^{6} cells.

Boundary conditions. Because experimentally measured velocity profiles were not available, special care was taken in developing the inlet boundary conditions. A portion of the digitized pipe surface immediately upstream of the section used for LES was used to develop the inlet profile for the LES. The upstream section, with $L/D = 5$, was modeled using a two layer, realizable $k - \varepsilon$ turbulence model (Shih et al. 1995) and streamwise periodic boundary conditions. After solving for the flow in the upstream pipe, the velocity distribution at the pipe outlet was exported and used to define the

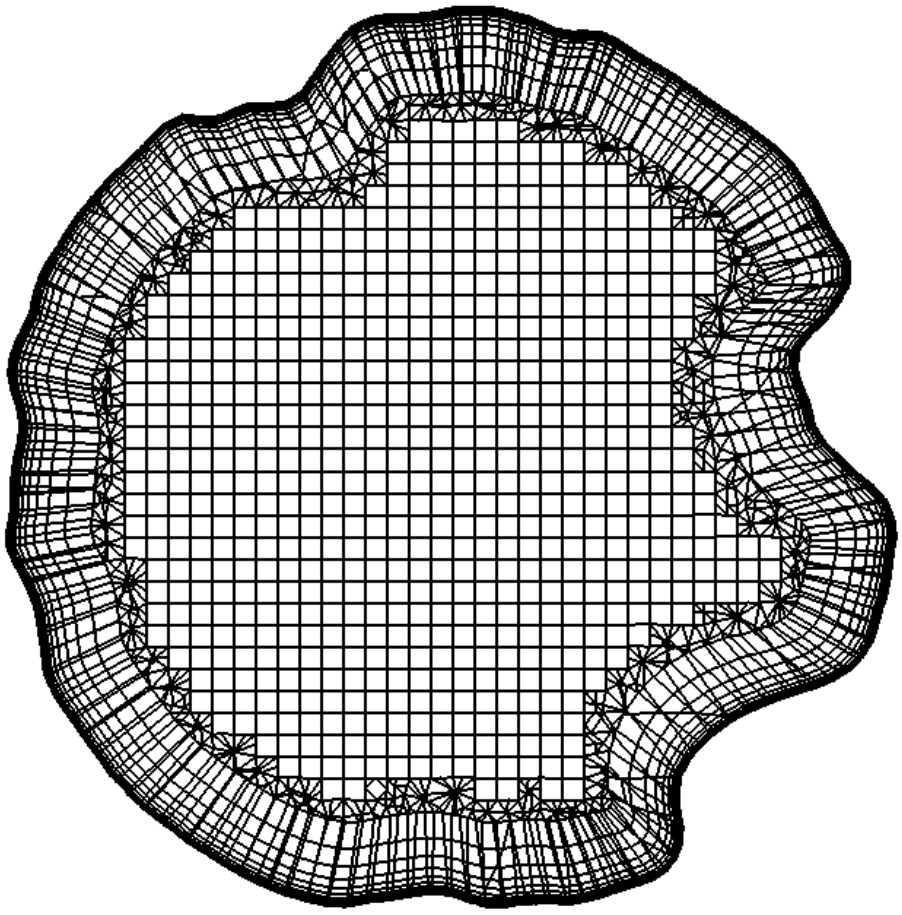

Figure 24: Cross-section of the volume mesh

inlet velocity profile of the downstream LES section. In order to provide an unsteady inlet profile, perturbations were added using the vortex method of Mathey et al. (2003).

Numerical method. The filtered Navier Stokes equations were solved using version 12.0.16 of the general purpose CFD code FLUENT (Fluent 2009). Bounded second-order central differencing was used to discretize the momentum term while diffusive terms were discretized using second-order central differencing. Pressure-velocity coupling was achieved using the fractional step method with non-iterative time

advancement. A time step of 0.0025-s was employed, and the normalized residuals of all discretized transport equations were reduced by 5 orders of magnitude for each time step.

The filtered Navier Stokes equations for an incompressible fluid are presented as

$$\frac{\partial \overline{u}_i}{\partial x_i} = 0 \tag{19}$$

and

$$\frac{\partial}{\partial t}(\rho\overline{u}_i) + \frac{\partial}{\partial x_j}(\rho\overline{u}_i\overline{u}_j) = \frac{\partial}{\partial x_j}\left(\mu\frac{\partial \sigma_{ij}}{\partial x_j}\right) - \frac{\partial \overline{p}}{\partial x_i}\frac{\partial \tau_{ij}}{\partial x_j} \tag{20}$$

where ρ is the density, t is the time, $\overline{u}_i$ ($i = 1, 2, 3$) is the filtered component of the velocity, μ is the dynamic viscosity, $\overline{p}$ is the pressure, and repeated indices indicate summation; σ_{ij} is the stress tensor due to molecular viscosity and τ_{ij} is the subgrid-scale stress defined by:

$$\sigma_{ij} = \left[\mu_t\left(\frac{\partial \overline{u}_i}{\partial x_j} + \frac{\partial \overline{u}_j}{\partial x_i}\right)\right] - \frac{2}{3}\mu\frac{\partial \overline{u}_l}{\partial x_l}\delta_{ij} \tag{21}$$

$$\tau_{ij} \equiv \rho\overline{u_i u_j} - \rho\overline{u}_i\overline{u}_j \tag{22}$$

The subgrid-scale stresses are a result of the filtering process and are unknown. The subgrid-scale model employed the Boussinesq hypothesis (cf. Hinze 1975) giving:

$$\tau_{ij} - \frac{1}{3}\tau_{kk}\delta_{ij} = -2\mu_t\overline{S}_{ij} \tag{23}$$

$$\delta_{ij} = \begin{cases} 0 & i \neq j \\ 1 & i = j \end{cases} \tag{24}$$

where δ_{ij} is the Kronecker delta, μ_t is the eddy viscosity (which is unknown and must be supplied by the subgrid-scale model), and $\overline{S}_{ij}$ is the rate-of-strain tensor for the resolved scale defined as

$$\overline{S}_{ij} \equiv \frac{1}{2}\left(\frac{\partial \overline{u}_i}{\partial x_j} + \frac{\partial \overline{u}_j}{\partial x_i}\right) \tag{25}$$

The subgrid scale model used in this study was developed by Germano et al. (1991) with subsequent refinement by Lilly (1992) and is commonly referred to as the dynamic Smagorinsky model. The basic assumption of the dynamic Smagorinsky model is that the small scales are in equilibrium so that energy production and dissipation are in balance. This assumption leads to the following expression for the eddy-viscosity:

$$\mu_t = \rho L_s^2 \left|\overline{S}\right| \tag{26}$$

where $|S| \equiv \sqrt{2\overline{S}_{ij}\overline{S}_{ij}}$ and L_s is the is the mixing length for subgrid-scales calculated as

$$L_s = min\left(\kappa d, C_s V^{1/3}\right) \tag{27}$$

where κ is the von Kármán constant, d is the distance to the closest wall, C_s is the Smagorinsky constant, and V is the volume of the computational cell. A test filter operation is performed giving resolved turbulent stresses, L_{ij}, as

$$\rho L_{ij} = \rho\widetilde{\overline{u_i u_j}} - \rho\widetilde{\overline{u}}_i\widetilde{\overline{u}}_j = T_{ij} - \tilde{\tau}_{ij} \tag{28}$$

where the ⎯ represents the grid filtered values and the $\widetilde{}$ represents the test filtered results. The model constant C_s is then defined as

$$C_s = -\frac{1}{2\Delta_f^2}\frac{L_{ij}M_{ij}}{M_{ij}M_{ij}} \tag{29}$$

where

$$M_{ij} = \frac{\tilde{\Delta}_f^2}{\Delta_f^2\left|\widetilde{\overline{S}}\right|\widetilde{\overline{S}}_{ij} - \left|\widetilde{\overline{S}}\right|\widetilde{\overline{S}}_{ij}} \tag{30}$$

and Δ_f is the filter width defined as $\Delta_f = V^{1/3}$. The subgrid-scale stresses computed dynamically in this manner are zero for laminar flow and asymptotically tend to zero in the near wall region. However, the coefficient field obtained using Equations 29 and 30 is highly variable with a significant percentage of negative values. Because this behavior can contribute to numerical instabilities, values of C_s are clipped so that $0 \leq C_s \leq 0.23$.

Results

Bulk Reynolds number was calculated as $\mathrm{Re} = U_{bulk} \cdot L_c/\nu$ where U_{bulk} represents the bulk (mean) velocity and L_c the characteristic length. The characteristic length was defined as $L_c = \sqrt{(4 \cdot \forall/L) \cdot \pi}$ where $\forall$ represents the volume of the solution domain and L represents the pipe length. Based on this definition the characteristic length represents the diameter of a circular pipe having the same volume

and length as the aged pipe. In this work, the characteristic length of the aged pipe was found to be 0.0507-m. The mean velocity was specified as 0.213-m/s with a kinematic viscosity of 1.59×10^{-6}-m/s^2, resulting in $\mathrm{Re} = 6800$.

During the solution process, mesh independence was assessed by first computing the results using a base-level mesh with approximately 1.7×10^6 cells, and then performing two separate mesh adaptations. In the first adaptation, the 3 cell layers adjacent to the wall boundary of the base-level mesh were refined to produce a mesh with approximately 3.6×10^6 cells. For the second adaptation, the cells with the largest root-mean-squared velocity fluctuations were refined to give a final mesh of 4.3×10^6 cells. Flow was then computed using each of the refined meshes, and the results were compared to the values obtained from the base-level mesh using drop in total pressure as the basis for comparison. The drop in total pressure computed using the base-level mesh was 12.4-Pa. The first refined mesh computed a drop of 12.8-Pa while the second computed a drop of 12.3-Pa, differences of approximately 3% and <1% from the base-level mesh, respectively.

Power spectral density is proportional to wavenumber raised to the -5/3 power ($E \propto k^{-5/3}$) throughout the inertial range (Kolmogorov 1941). In order to validate the LES, plots of the power spectral density were created. Time series data of the instantaneous x-component of velocity was recorded at three points within the solution domain for approximately 11 through-flow times (TFT) where the through-flow time is defined as $TFT = L/U_{bulk}$. The three points were located at the centroid of the pipe

cross section, halfway between the centroid and the pipe wall ($r/R \sim 0.5$), and near the pipe wall ($r/R \sim 0.95$). Fourier analysis was used to obtain plots of power spectral density versus wavenumber from the times series data. Figure 25 is a log-log plot of the power spectral density at the centroid of the pipe cross-section and includes a central weighted moving average of the power spectral density data points. For comparison, a line with a slope of -5/3 is shown. The linear portion of the plot of power spectral density is very close to theoretical value. In addition, the spectral plots obtained from the monitoring points at $r/R \sim 0.5$ and $r/R \sim 0.95$ were similar.

The ability of LES to reproduced laboratory results was evaluated in terms of the Darcy-Weisbach friction factor. The laboratory results gave a friction factor of 0.113 while the LES results gave a friction factor of 0.090. While the LES results represent a

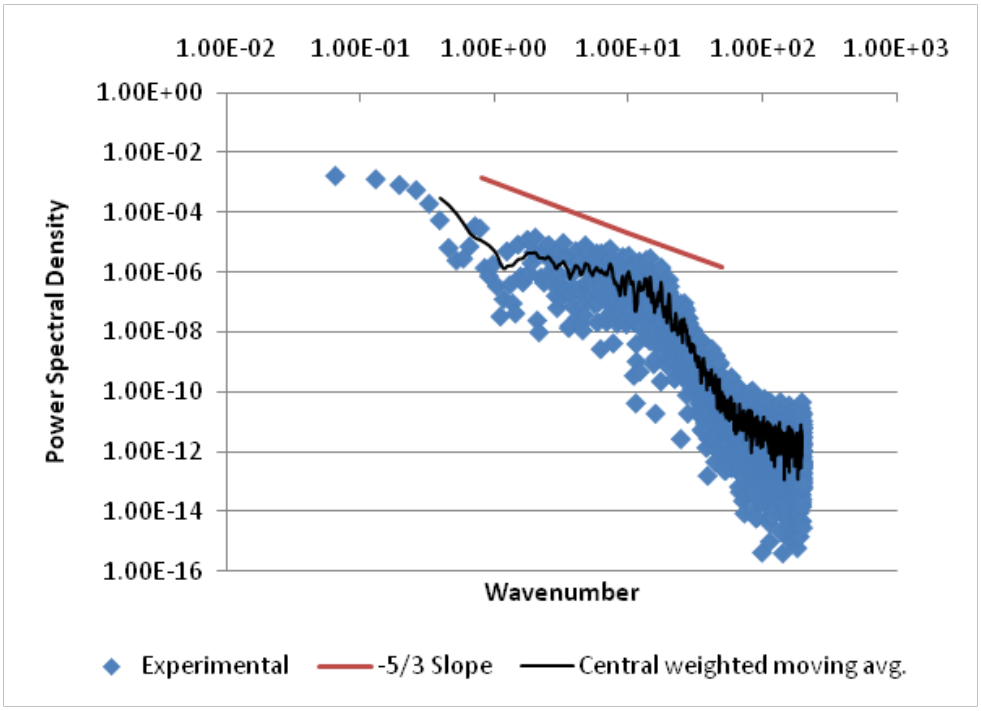

Figure 25: Power spectral density at the centroid of the cross-section

20% deviation as compared to the laboratory data, results with similar accuracy may be satisfactory for many applications. Several possible explanations exist for the underprediction of the friction factor. The most prominent are: the section modeled using LES was too short to be representative of the much longer laboratory test section, the inability to resolve the smallest scale roughness elements, and possible deficiencies in the subgrid-scale model for describing complex flows. Each of these possibilities will be addressed in the following paragraphs.

As noted, the length of the pipe used in the LES was limited to $L/D = 6$. In contrast, the length of the laboratory tested pipe section was $L/D = 56$. Because of the irregular nature of the roughness in the aged pipe, it is worthwhile to consider whether the pipe section used for the LES was representative of the laboratory tested section. To facilitate comparison, the $k - \varepsilon - v^2 - f$ model of Lien and Durbin (1996) was employed to compute flow through the same aged pipe as modeled using LES but with a length of $L/D = 22$. The mesh utilized for $k - \varepsilon - v^2 - f$ modeling consisted of 4×10^6 mixed cells. Similarly to the LES, the boundary layer was resolved using prismatic elements; however, for the $k - \varepsilon - v^2 - f$ model the bulk of the interior volume was meshed using tetrahedral elements. Furthermore, the approach in developing boundary conditions for the $k - \varepsilon - v^2 - f$ model was comparable to the approach outlined previously for the LES. With the mesh and boundary conditions defined in this manner, the $k - \varepsilon - v^2 - f$ model was very accurate at reproducing the laboratory calculated friction factors, giving a friction factor of 0.115 (a 2% increase over laboratory

results). However, if only the $L/D = 6$ section utilized in performing the LES is considered, the $k - \varepsilon - v^2 - f$ model produces a friction factor of 0.131, suggesting that the shorter pipe section modeled using LES is actually rougher than the average roughness of the longer pipe section that was tested in the laboratory. Figure 26 is a plot of the total pressure drop versus axial pipe position for the $L/D = 6$ section using LES and the $k - \varepsilon - v^2 - f$ turbulence model. Total pressure drop within the pipes does not occur at a constant rate, but rather varies depending on location within the pipe. However, Figure 26 illustrates that the variation is relatively small when compared to the total drop over the modeled length of pipe. For these reasons the short length of the modeled section is not believed to be a primary cause of the underprediction of the friction factor by LES.

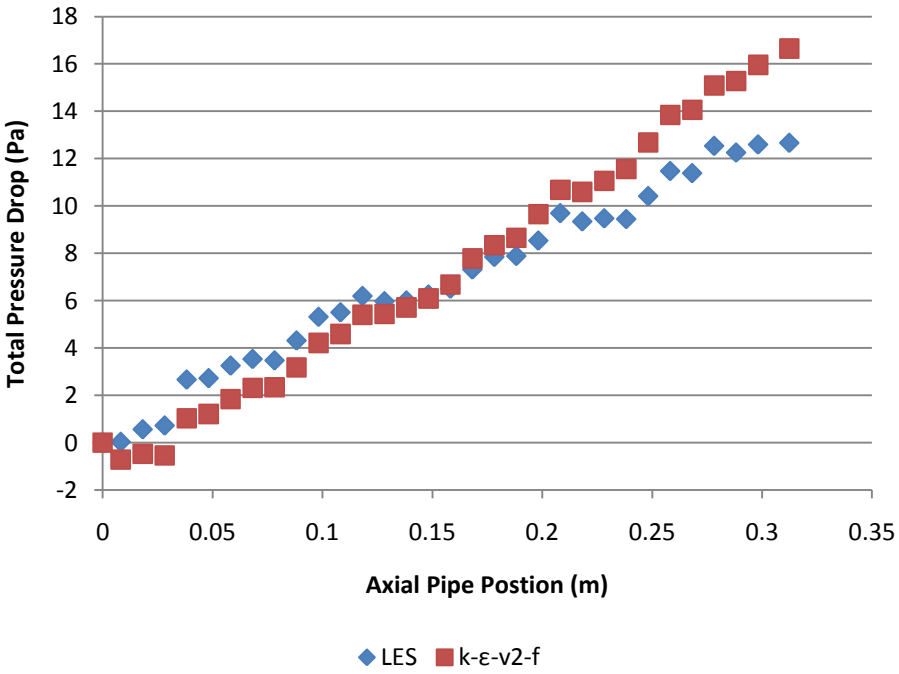

Figure 26: Total pressure drop versus axial position

The Moody diagram (Moody 1944) will be used in order to consider the potential effects of the roughness elements that were too small to be resolved by the surface mesh. The Moody Diagram shows the Darcy Weisbach friction factor for a smooth pipe at $\mathrm{Re} = 6800$ to be 0.034. Therefore, a smooth pipe with the same pipe diameter, length, and flow conditions as utilized in the LES will have pressure drop of 4.75-Pa. In contrast, a pipe with a roughness height of 1-mm (a general value for rusted cast iron pipe before the onset of significant tuberculation) would have a Darcy-Weisbach friction factor of 0.054 resulting in a pressure drop of 7.51-Pa, increases of 0.02 in friction factor and 2.76-Pa in pressure loss over the smooth pipe. The difference in pressure drop between a smooth pipe and a pipe with a 1-mm roughness height is very close to the magnitude of the underprediction of the LES. Nonetheless, it should be noted that the roughness values from this simplified analysis should not be expected to be additive with the LES results, but rather the relationship is much more complex. Instead, this analysis demonstrates that errors associated with roughness element filtering are of the proper order of magnitude to explain the underprediction of the LES.

The final source of potential error that will be discussed is deficiency in the subgrid-scale model formulation. The dynamic Smagorinsky model (Lilly 1992) has been used extensively since its development; nonetheless, as noted previously, Equations 29 and 30 produce highly variable coefficient fields and require clipping or damping in order to maintain model stability. Several researchers (cf. Ghosal et al. 1995; Meneveau et al. 1996; Vreman 2004) have recognized that the highly variable coefficient field with

the associated clipping and damping functions limit the applicability of the dynamic Smagorinsky model to complex flows. As the flow in this study is three-dimensionally complex, it is reasonable to suppose that a more advanced sub-grid scale model may improve results.

In order to present the flow characteristics calculated by LES, contour plots have been included. Figure 27 is a plot of the mean velocity magnitude normalized by the bulk velocity. The effects of the irregular boundary are clearly visible as the contours are highly distorted. Still, the overall profile is in line with expectations for a turbulent velocity profile; the velocity gradient is high near the wall boundary and relatively low throughout the core flow region. Figures 28 and 29 are radial and longitudinal plots of

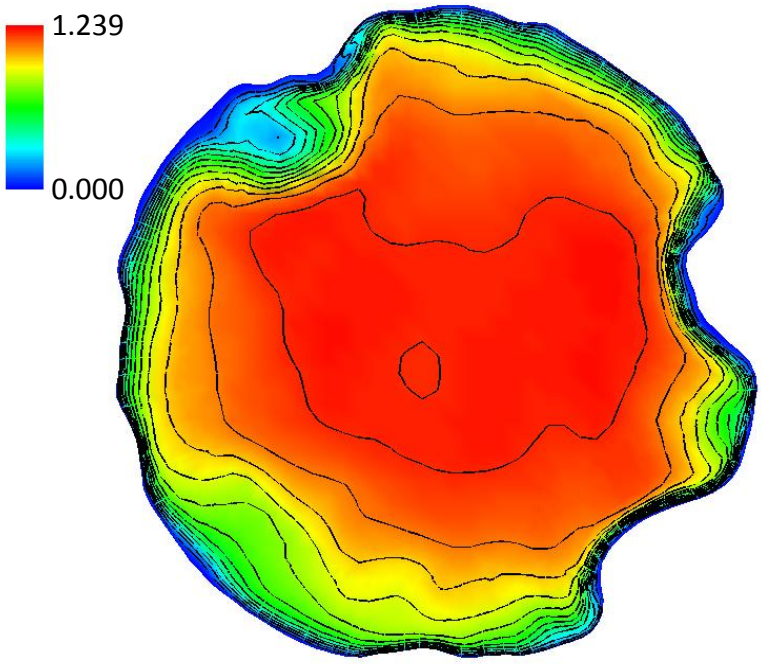

Figure 27: Mean velocity magnitude normalized by bulk velocity. contours – min = 0, max = 1.20, interval = 0.1

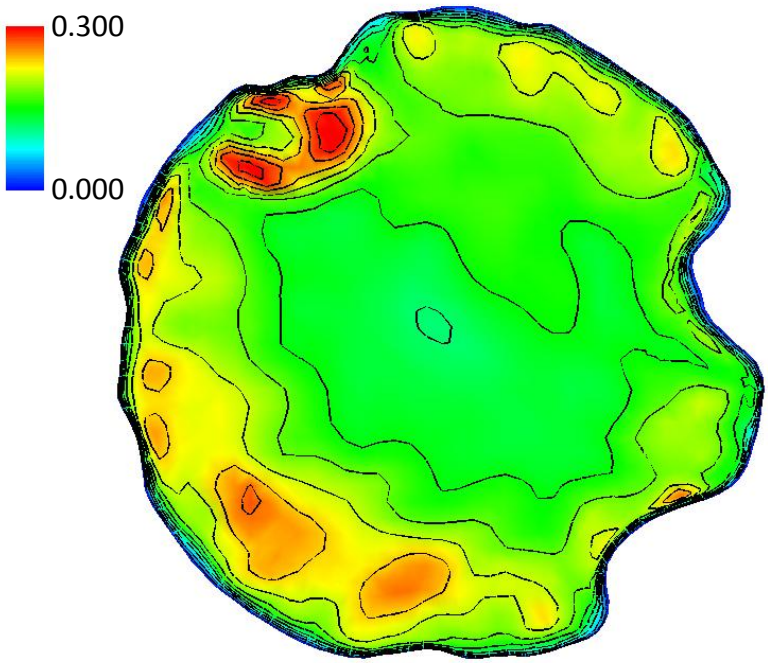

Figure 28: Root mean square velocity fluctuations normalized by bulk velocity. contours – min = 0, max = 0.30, interval = 0.03

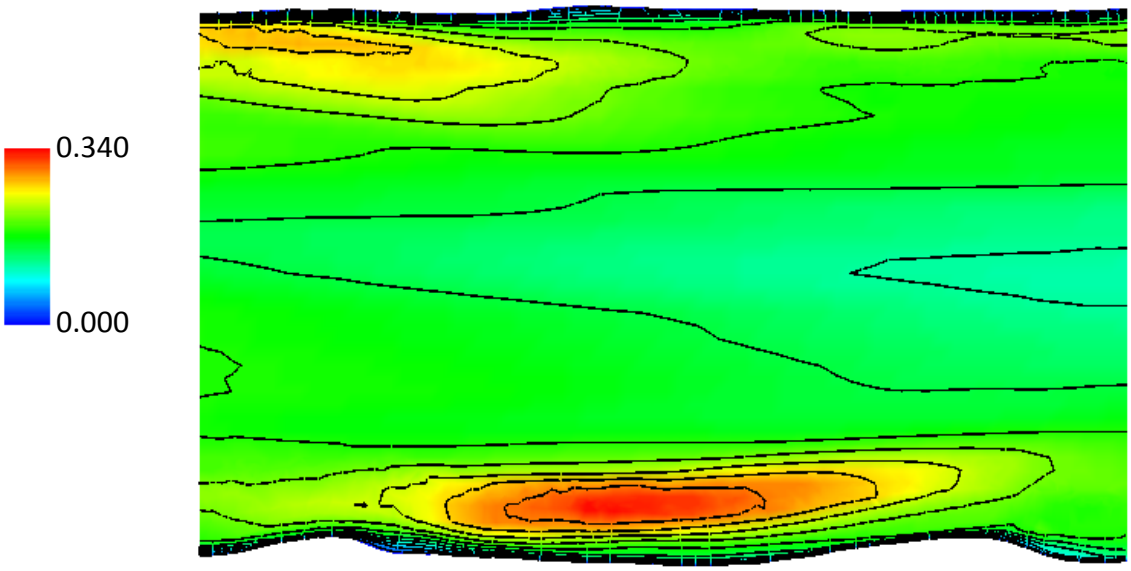

Figure 29: Longitudinal plot of root mean square velocity fluctuations normalized by bulk velocity. contours –min = 0, max = 0.3, interval = 0.03

the root mean square velocity fluctuations normalized by the bulk velocity. The largest velocity fluctuations occur at a small distance from the pipe wall. The radial plot demonstrates how the locations of the maxima are irregularly spaced around the exterior of the pipe. Similarly, the longitudinal plot illustrates the variation in the streamwise direction. All of the plots exhibit irregularity as a result of the three-dimensional nature of the wall boundary.

Conclusion

LES can be a powerful aid in understanding the flow dynamics of aged pipes. The ability of LES to describe turbulent fluctuations is particularly important in understanding processes such as dissolved material transport, suspended particle accretion and erosion, and fluid mixing, where turbulence plays a significant role. Despite the utility of LES for describing flow, this is believed to be the first application to aged pipes with three-dimensional, irregular boundaries. In this study LES produced friction factors about 20% lower than experimentally measured values. Considering the complexity of the modeled pipe, and the degree to which the pipe has changed, the LES produced friction factor still represents a good estimate of the aged pipe friction, and likely has sufficient accuracy for many applications. Nevertheless, the weaknesses of LES as applied to aged pipes are highlighted in this analysis. Three primary areas of concern were identified: the short length of the pipe section used in LES, the unresolvable roughness elements, and the subgrid-scale model. Upon further review,

the unresolvable roughness elements and the subgrid-scale model were identified to be the most likely impediments to obtaining more accurate LES results.

Additional testing would help to determine more precisely the strengths and weakness of LES as applied to the irregular boundaries of aged pipes. Testing additional pipes of different sizes and multiple flow rates would help to better establish the accuracy of LES in aged pipes. Increasing the length of test sections will help eliminate bias that may occur as a result of testing short pipe sections. Similarly, performing LES using multiple subgrid-scale models will help to validate which models perform the best for complex flows.

CHAPTER VI

SUMMARY AND CONCLUSIONS

Summary

The general purpose of this research was to improve the accuracy of network distribution models. In order to achieve this goal, the following intermediate objectives were identified:

1. Evaluate the changes that occur in aged pipes with respect to hydraulic roughness and flow area
2. Assess the capability of CFD for modeling the complex flow of pipes with irregular three-dimensional boundaries
3. Evaluate how the changes in aged pipes found for Objective 1 affect the hydraulics within a pipe network
    a. Macro-scale (distribution wide)
    b. Micro-scale (< 1-m)
4. Develop a method for predicting the effective diameter of a pipe based on its roughness and original diameter
5. Determine the effects of aging on distribution system performance using a simplified model of an existing network

Each of the study objectives has been addressed through the use of network and CFD modeling.

The development of accurate network models has become an important part of understanding the operation of distribution systems. However, the changes that take place in distribution systems greatly complicate network modeling. These changes can largely be overcome through a process of careful calibration. The first step in improving the calibration of network models of systems containing aged pipes is to obtain an understanding of how pipes change with age. The preliminary laboratory testing answered that question by evaluating the changes that occurred in the hydraulic roughness and flow area of aged pipes (Objective 1). Next, the results from the preliminary laboratory testing were used to develop a method for predicting the effective diameter of a pipe based on its roughness and original diameter (Objective 4). Application of these findings during the calibration of a sample network model demonstrated the effects of aging on distribution hydraulics and overall system performance (Objectives 3.a and 5).

CFD modeling, on the other hand, was used during this study to providing highly detailed descriptions of flow through two aged pipe sections. During the course of this study CFD has been found capable of modeling the complex flow that occurs in pipes with irregular three-dimensional boundaries (Objective 2). Processes such as disinfection byproduct formation and transport, suspended material transport, and flow mixing have been identified as potential beneficiaries of the increased data obtainable from CFD. While the CFD results from the current study have not been directly applied to network modeling, the utility of CFD for describing complex flow has been

demonstrated to be a useful tool for analyzing the hydraulics of aged pipes (Objective 3.b).

Conclusions and Recommendations

Contributions. Meeting the objectives for this study has resulted in several noteworthy contributions with respect to network and CFD modeling. The specific contribution can be listed as follows:

1. The effect of aging pipes on distribution hydraulics has been outlined with respect to modeling correct water age
2. A method for correcting the diameters of aged pipes has been described
3. CFD has been used to compute flow in an aged pipe for the first time
    a. RANS
    b. LES
4. CFD has been demonstrated to be a useful method for describing flow over small sections of three-dimensionally irregular pipes

The first two contributions were achieved by applying the laboratory results to in performing network modeling, while the final two were addressed by the CFD modeling. The following sections discuss the conclusions and recommendation for each type of model within the context of the study contributions.

Network modeling. The roughness and diameter changes in eleven aged pipes were measured. By utilizing the laboratory results to adjust the pipe diameters in a network distribution model, errors in peak water age of 6.7 to 8.4% were observed as a

consequence of disregarding the changes that occur in the diameter of aged pipes. Meanwhile, errors of 7.2 to 10% were noted for minimum water age. While the magnitude of these errors may not be large when considering the uncertainty that may exist in a network distribution model, the errors are systematic in nature. Whenever possible, systematic error should be minimized. The variable with the largest effect on the water age at a location within the sample distribution network was the operational status of the water tank: whether water was flowing into the tank, or out of the tank. Reducing pipe diameter significantly changed the timing of the maxima and minima in water age by reducing the overall travel time of water in the distribution system. It was demonstrated that looping pipe structures within the network along with the associated mixing that occurs at nodes can result in situations where the variation of water age as a function of time is completely changed by reducing pipe diameters.

The method outlined for applying diameter corrections in calibrating distribution networks is efficient. A modeler can first calibrate a network based on flow distribution and headloss and then review whether diameter corrections are justifiable based on pipe roughness. If diameter reductions are judged to be necessary, the corrections can be instituted in a single step without changing the flow distribution or headloss in a model; only the flow velocity is altered. Nevertheless, modelers should be cautious whenever altering the physical attributes of distribution model components. Making a change in the model that does not represent the physical reality of the network introduces rather than eliminates error. Modelers should be especially wary of using

the data in this study for pipes that are outside of the size range of the pipes analyzed for this study or for cases where the process causing increased roughness and diameter reduction in the pipes is different than the iron corrosion noted in these pipes.

The pipe network example has demonstrated the utility of relating roughness to d/D. In order to further strengthen the previously presented relationship between roughness and d/D, more aged pipe roughness tests and volume tests are necessary. Tests on larger pipes and pipes with different types of buildup would be especially useful. Moreover, the most complete validation of the utility of adjusting aged pipe diameters would be to develop a water distribution model using the specified diameter reductions and compare model output to data obtained from field testing of the actual distribution system.

CFD modeling. CFD modeling has the potential to improve the understanding of many of the flow mechanics in aged pipes. Despite the widespread usage of aged pipes, very few numerical studies have focused on pipes that have three-dimensional irregular roughness. Obtaining accurate surface representations, meshing the computational domain, and model convergence are all complicated by irregular boundary surfaces. Nevertheless, CFD modeling can potentially offer much insight into the flow phenomena that occur in aged pipes. Water quality modeling, in particular, has much to gain from an improved understanding of the flow in rough pipes.

The $v^2 - f$ turbulence model was the most accurate of the three RANS models at matching the headloss measured from the laboratory testing. Performance of the

$v^2 - f$ model was best for the 0.050-m pipe at $\mathrm{Re} = 6700$ where the Darcy-Weisbach friction factor was over predicted by 5% as compared to laboratory data. Interestingly, for every other flow scenario the friction factor was under predicted by the RANS models. For the 0.025-m pipe at $\mathrm{Re} = 13{,}000$, the $v^2 - f$ turbulence model under predicted the Darcy-Weisbach friction factor by about 14% while for the 0.050-m pipe at $\mathrm{Re} = 31{,}000$ the Darcy-Weisbach friction factor was under predicted by about 15%. Because form drag was the dominant resistive force in the aged pipes, deficiencies in calculating flow separation are a likely culprit for the near-universal under prediction of friction factor. The inability of the boundary meshes to resolve the smallest variations surface roughness may also play a more minor role in the under prediction of friction factor.

The $v^2 - f$ turbulence model was also more accurate than LES at predicting the Darcy-Weisbach friction factor of the 0.050-m pipe as the LES under predicted the friction factor by 20%. Despite the superiority of the $v^2 - f$ model at predicting friction factors, LES still has advantages in describing processes where turbulent fluctuations are important. Perhaps the most likely source of error in the LES is the subgrid-scale modeling. While the dynamic Smagorinsky subgrid-scale model (Germano et al. 1991; Lilly 1992) used in this study has been widely used since its development, the flow addressed in this work is highly complex and an improved subgrid-scale model may be required to obtain better results.

Despite current limitations, CFD modeling has been shown to be a powerful tool in better understanding flow in aged, rough pipes. The current testing demonstrates the importance of modelers being aware of the limitations of CFD in describing complex flows at high Reynolds numbers. While imperfect, these tests indicate that CFD modeling can be used successfully to model flow in aged pipes. Without CFD, it is very difficult to obtain information on the turbulence parameters and velocity profiles of aged pipes.

Several areas of the CFD modeling would benefit from further study. In the current study only a handful of Reynolds numbers were considered. Further research should evaluate the capabilities of CFD models over an expanded range of Reynolds numbers with a specific emphasis on higher values. In addition, modeling larger pipes would further expand the data set. The principal goal of the CFD modeling in this work has been to evaluate the accuracy of CFD in modeling complex flows in aged pipes. The next step is to use the CFD models in order to better understand the transport processes, fluid mixing, etc. that occur in aged pipes.

REFERENCES

Acharya, S., Dutta, S., Myrum, T. A., and Baker, R. S. (1994). “Turbulent flow past a surface-mounted two-dimensional rib.” *ASME J. Fluids Eng.*, 116(2), 238-246.

ASME (American Society of Mechanical Engineers) (2004). *Welded and seamless wrought steel pipe*. B36.10M – 2004, New York.

AWWA (American Water Works Association) (2005). *Computer modeling of water distribution systems*, Denver, Colorado.

AWWA and EES (Economic and Engineering Services, Inc) (2002). “Effects of water age on distribution system water quality.” <http://www.epa.gov/safewater/disinfection/tcr/pdfs/whitepaper_tcr_waterdistribution.pdf>, June 6, 2009.

AwwaRF (Awwa Research Foundation) (2004). *Predictive models for water quality in distribution systems*, Denver, Colorado.

Boersma, B. J., and Nieuwstadt, F. T. M. (1996). “Large-eddy simulation of turbulent flow in a curved pipe.” *ASME J. Fluids Eng*., 118(2), 248-254.

Boxall, J. B., Saul, A. J., and Skipworth, P. J. (2004). “Modeling for hydraulic capacity.” *J. AWWA*, 96(4), 161-169.

Christensen, R. T. and Barfuss, S. L. (2009). “Improving water quality modeling in systems containing tuberculated pipes.” *Proc., Annual Conference and Exposition 2009*, AWWA, San Diego, CA.

Clark, R. M. and Haught, C. H. (2005). “Characterizing pipe wall demand: Implications for water quality modeling.“ *J. Water Resour. Plan. Manage*., 131(3), 208-217.

Colebrook, C. F. and White, C. M. (1937a). “The reduction of carrying capacity of pipes with age.“ *Jour. Inst. Civil Engrs.*, 7(1), 99-118.

Colebrook, C. F. and White, C. M. (1937b). “Experiments with fluid friction in roughened pipes.” *Proceedings of the Royal Society*, 161(906), 367-381.

Eggels, J. G. M. (1994). "Direct and large eddy simulation of turbulent flow in a cylindrical pipe geometry," Ph.D. Thesis, Delft University Press, Delft, The Netherlands.

Eggels, J. G. M. and Nieuwstadt, F. T. M. (1993). "Large-eddy simulation of turbulent flow in an axially rotating pipe." *Proc. of the 9th Symp. on Turbulent Shear Flows*, Kyoto, Japan.

Feiz, A. A., Ould-Rouis, M., and Lauriat, G. (2002). "Large eddy simulation of turbulent flow in a rotating pipe." *J. Heat Fluid Flow*, 24(3), 412-420.

Fluent, Inc. (2006). *Fluent 6.3 Users Guide*, Lebanon, N.H.

Fluent, Inc. (2009). *Fluent 12.0 Users Guide*, Lebanon, N.H.

Germano, M.,Piomelli, U., Moin, P., and Cabot, W. H. (1991). "A dynamic subgrid-scale viscosity model." *Phys. Fluids A*, 3(7), 1760-1765.

Ghosal, S., Lund, T. S., Moin, P. and Akselvoll, K. (1995). "A dynamic localization model for large-eddy simulation of turbulent flow," *J. Fluid Mech*, 286, 229-255.

Hallam, N. B., West, J. R., Forster, C. F., Powell, J. C., and Spencer, I. (2002). "The decay of chlorine associated with the pipe wall in water distribution systems." *Water Res.*, 36(14), 3479-3488.

Hinze, J. O. (1975) *Turbulence*, McGraw-Hill, New York.

Hirrel, T. D. (2008). "How not to calibrate a hydraulic network model." *J. AWWA*, 100(8), 70-81.

Khan, L. A., Wicklein, E. A., Teixeira E. C. (2006). "Validation of a three-dimensional computational fluid dynamics model of a contact tank." *J. Hydraul. Eng.* 132(7). 741-746.

Kolmogorov, A. N. (1941). "The local structure of turbulence in incompressible viscous fluid at very high Reynolds number." *Dokl. Akad. Nauk SSSR*, 30, 301-305.

Krogstad, P. (1991). "Modification of the van Driest Damping Function to Include the Effects of Surface Roughness, *AIAA J.*, 29(6), 888-894.

Lamont, P. A. (1981). "Common pipe flow formulas compared with the theory of roughness." *J. AWWA*, 73(5), 274-280.

Lien, F. S., and Durbin (1996). "Non-linear $k-\varepsilon-v^2$ modeling with application to high lift." *Proc. of the Summer Program*, Center for Turbulence Research, Stanford, Calif., 5-22.

Lilly, D. K. (1992). “A proposed modification of the Germano subgrid-scale closure method.” *Phys. Fluids A*, 4(3), 633-635.

Mahmood, G. I., Hill, M. L., Nelson, D. L., Ligrani, P. M., Moon, H.-K., and Glezer, B. (2001). “Local heat transfer and flow structure on and above a dimpled surface in a channel.” *ASME J. Turbomachinery*, 123(1), 115-123.

Mahmud, S., Islam, A. K. M. S., Feroz, C. M. (2003). “Flow and heat transfer characteristics inside a wavy tube.” *Heat and Mass Transfer*, 39, 387-393.

Mamrelli, E. S., and Streicher, L. (1962). “Loss in capacity of water mains: California Section Committee Report.” *J. AWWA*, 54(10), 1293-1312.

Mathey, F., Cokljat, D., Bertoglio, J. P., and Sergent, E. (2003). “Specification of LES inlet boundary condition using vortex method.” *4th Int. Symp. on Turbulence, Heat and Mass Transfer*, Antalya, Turkey.

McCoy, A., Constantinescu, G., Weber, L. (2008).”Numerical investigation of flow hydrodynamics in a channel with a series of groynes.” *J. Hydraul. Eng.*, 134(2), 157-172.

Meneveau, C., Lund, T. S., and Cabot, W. H. (1996). “A Lagrangian dynamic subgrid-scale model of turbulence,” *J. Fluid Mech*, 319, 353-384.

Michel, R., Quemard, C., and Durant, R. (1968). “Hypothesis on the mixing length and application to the calculation of the turbulent boundary layers.” *Proc., Computation of Turbulent Boundary Layers - 1968 AFOSR-IFP-Stanford Conference*, Stanford University, Stanford, Calif., 195–207.

Moin P., and Mahesh K. (1998).”Direct Numerical Simulation: A Tool in Turbulence Research.” *Annu. Rev. Fluid Mech*. 30, 539-578.

Moody, L. F. (1944). “Friction Factors for Pipe Flow,” *Trans. ASME*, 66, 671-684.

Nikuradse, J. (1933). “Stromungsgesetze in ruahen Rohren.” *VDI Forschungsh*., 361.

NRC (National Research Council) (2006). *Drinking Water Distribution Systems: Assessing and Reducing Risks*, National Academies of Sciences, Washington, D.C.

Park, J., and Ligrani, P. M. (2005). “Numerical predictions of heat transfer and fluid flow characteristics for seven different dimpled surfaces in a channel.” *Numer. Heat Transfer A*, 47, 209-232.

Patankar, S. V., Ivanovich, M., and Sparrow, E. M. (1979). "Analysis of turbulent flow and heat transfer in internally finned tubes and annuli." *ASME J. Heat Transfer*, 101, 29-37.

Patel, V. C. (1998). "Perspective: Flow at high Reynolds number and over rough surfaces – Achilles heel of CFD." *ASME J. Fluids Eng*., 120(3), 434-444.

Piomelli, U. (1999). "Large-eddy simulation: Achievements and challenges." *Prog. Aero. Sci.*, 35(4), 335-362.

Prandtl, L. (1933). "Neuere Ergebnisse der Turbulenxforschung." *Zeit. Ver. deu. Ing*., 77(5), 105-114.

Rhodes, D. G., and Senior, A. K. 2000. "Numerical study of resistance with rib roughness of various scales." *J. Hydraul. Eng.* 126(7). 541-546.

Rotta, J. C. (1962). "Turbulent boundary layers in incompressible flow." *Prog. Aero. Sci.*, 2(1), 1-95.

Rudman, M., and Blackburn, H. M. (1999). "Large eddy simulation of turbulent pipe flow." *2nd Int. Conf. on CFD in the Minerals and Process Industries*, Melbourne, Australia.

Russ, G., and Beer, H. (1997). "Heat transfer and fluid flow in a pipe with sinusoidal wavy surface – I. Numerical investigation." *Int. J. Heat Mass Transfer*, 40, 1061-1070.

Sharp, W. W., and Walski, T. M. (1988). "Predicting internal roughness in water mains." *J. AWWA*, 80(11), 34-40.

Shih, T.-H., Liou, W. W., Shabbir, A., and Zhu, J. (1995). "A new $k - \varepsilon$ eddy-viscosity model for high Reynolds number turbulent flows – Model development and validation." *Computers and Fluids*, 24, 227-237.

Skipworth, P. J.; Machell, J.; and Saul, A. J. (2002). "Empirical travel time estimation in a distribution network." *Water, Maritime and Energy*, 154(1), 41-49.

Smagorinsky, J. S. (1963). "General circulation experiments with the primitive equations." *Mon. Weather Review*, 91(3), 91-164.

Stoesser, T., Braun, C., García-Villalba, M., and Rodi, W. (2008). "Turbulence structures in flow over two-dimensional dunes." *J. Hydraul. Eng.*, 134(1), 42-55.

Teruzzi, A., Ballio, F., and Armenio, V. (2009). “Turbulent stresses at the bottom surface near an abutment: Laboratory-scale numerical experiment.” *J. Hydraul. Eng.*, 135(2), 107-117.

Unger, F., and Friedrich, R. (1991). “Large eddy simulation of fully-developed turbulent pipe flow.” *8th Symp. on Turbulent Shear Flows*, Munich, Germany.

USEPA (2008). *FACTOIDS: Drinking water and ground water statistics for 2008*, EPA 816-K-08-004, Washington, D.C.

USEPA. (2000). *EPANET 2.0., EPA water supply & water resources*. <http://www.epa.gov/ORD/NRMRL/wswrd/epanet.html>, Nov. 9, 2009.

van Driest, E. R. (1956). "On turbulent flow near a wall." *J. Aeronaut Sci.*, 23, 259-264.

Vijiapurapu, S., and Cui, J. (2006). “Simulation of turbulent flow in a ribbed pipe using large eddy simulation.” *Numer. Heat Transfer A*, 51, 1137-1165.

Vreman, A. W. (2004). “An eddy-viscosity subgrid-scale model for turbulent shear flow: Algebraic theory and applications,” *Phys Fluids*, 16(10), 3670-3681.

Walski, T. M. (2004). “Discussion: Modeling for hydraulic capacity.” *J. AWWA*, 96(10), 104-108.

Wang, H., and Falconer, R. A. (1998). “Numerical modeling of flow in chlorine disinfection tanks.” *J. Hydraul. Eng.* 124(9). 918-931.

Wilcox, D. C. (1998). *Turbulence modeling for CFD*, 2nd ed., DCW Industries, La Canada, Calif.

Williams, G. S., and Hazen, A. (1960). *Hydraulic tables*, Wiley, New York.

Wolfshtein, M. (1969). “The velocity and temperature distribution on one-dimensional flow with turbulence augmentation and pressure gradient.” *Int. J. Heat Mass Transfer*, 12, 301-318.

Yang Z. and McGuirk, J.J. (1999). “LES of rotating turbulent pipe flow with two subgrid-scale models.” *Proc. of the 1st Int. Symp. on Turbulence and Shear Flow Phenomena*, S. Banerjee and J. K. Eaton, eds., Santa Barbara, Calif.

Yucel, N., and Dinler, N., 2006. “Numerical study of laminar and turbulent flow through a pipe with fins attached.” *Numer. Heat Transfer A*, 49(2), 195-214.

Zeitoun, O., and Hegazy, A. S. (2003). “Heat transfer for laminar flow in internally finned pipes with different fin heights and uniform wall temperature.” *Heat Mass Transfer*, 40, 253-259.

APPENDIX

Appendix: Supplementary Figures

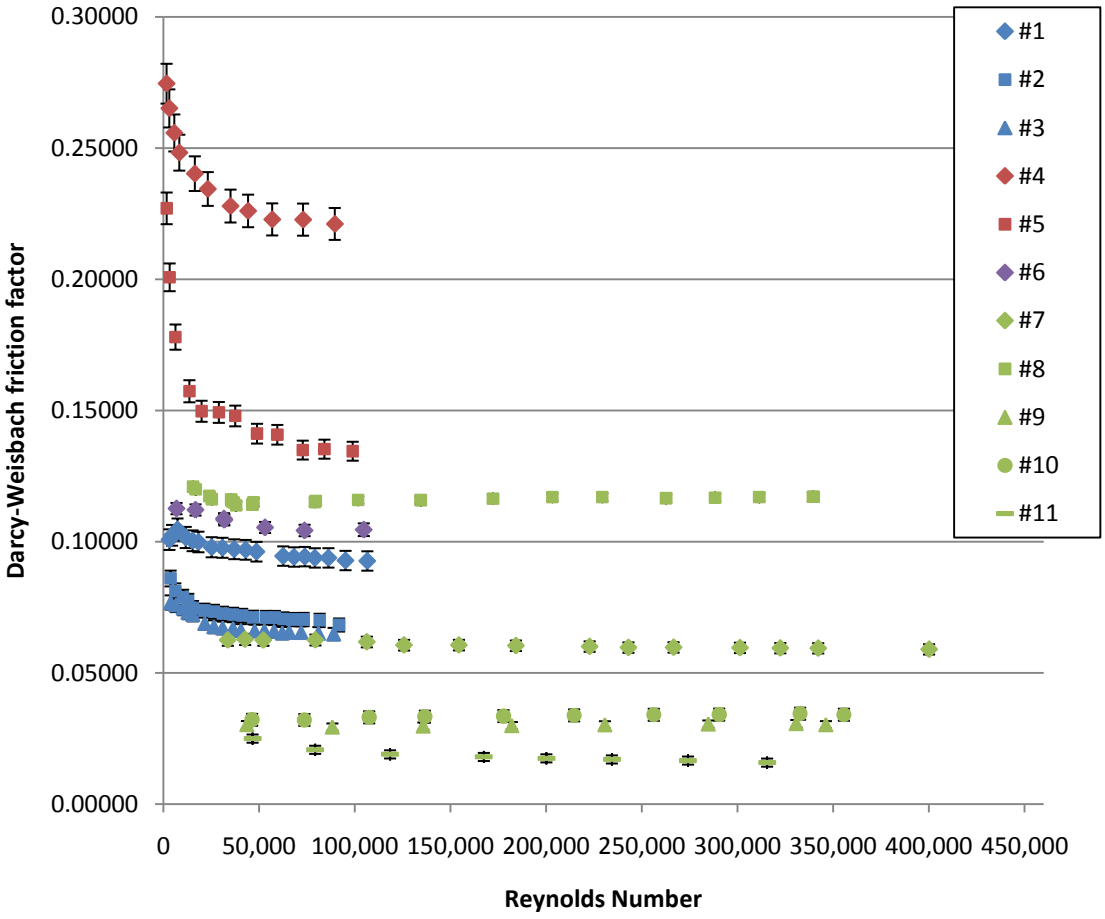

Figure 30: Plot of the Darcy-Weisbach friction factor versus Reynolds number with confidence intervals

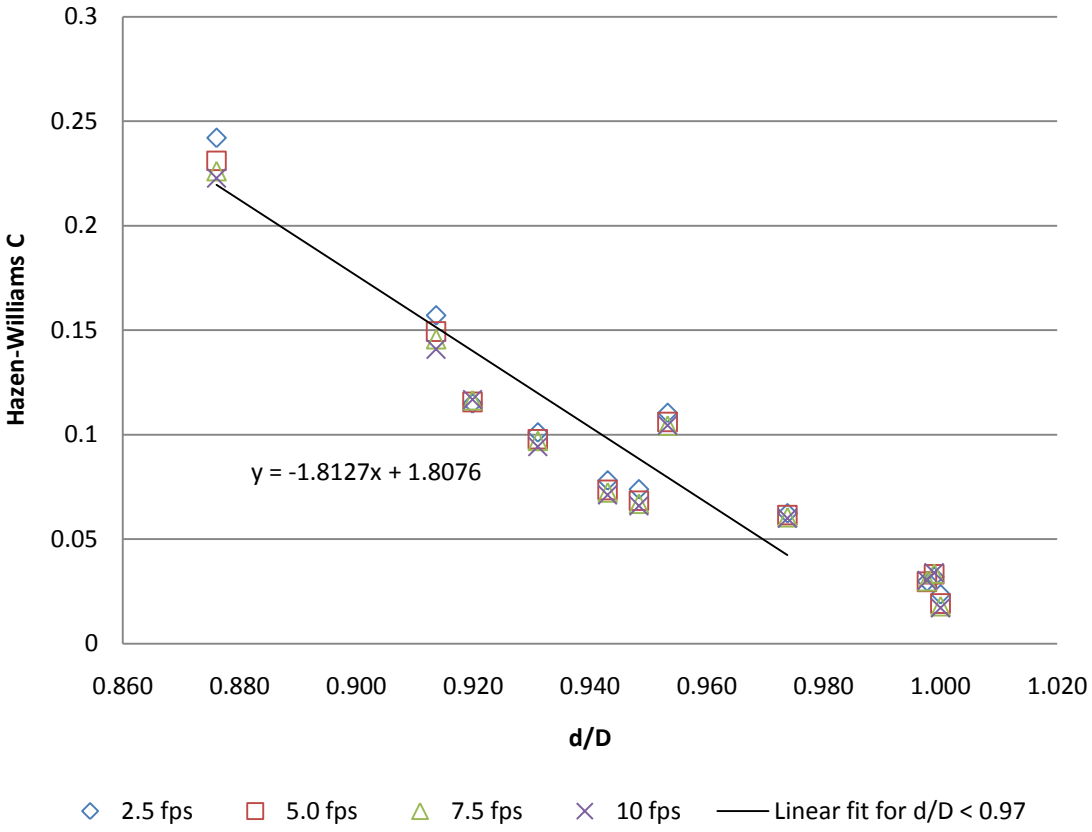

Figure 31: Plot of d/D versus Darcy-Weisbach friction factor